CORNEA MICROSTRUCTURAL AND MECHANICAL RESPONSE MEASURED USING NONLINEAR OPTICAL AND OPTICAL COHERENCE MICROSCOPY WITH SUB-10-FEMTOSECOND PULSES

A Dissertation

by

QIAOFENG WU

Submitted to the Office of Graduate Studies of
Texas A&M University
in partial fulfillment of the requirements for the degree of

DOCTOR OF PHILOSOPHY

May 2010

Major Subject: Biomedical Engineering

CORNEA MICROSTRUCTURAL AND MECHANICAL RESPONSE MEASURED USING NONLINEAR OPTICAL AND OPTICAL COHERENCE MICROSCOPY WITH SUB-10-FEMTOSECOND PULSES

A Dissertation

by

QIAOFENG WU

Submitted to the Office of Graduate Studies of
Texas A&M University
in partial fulfillment of the requirements for the degree of

DOCTOR OF PHILOSOPHY

Approved by:

Chair of Committee,	Alvin T. Yeh
Committee Members,	Jay D. Humphrey
	Brian E. Applegate
	Gheorghe Stoica
Head of Department,	Gerard L. Cote

May 2010

Major Subject: Biomedical Engineering

ABSTRACT

Cornea Microstructural and Mechanical Response Measured Using Nonlinear Optical and Optical Coherence Microscopy with Sub-10-femtosecond Pulses. (May 2010)

Qiaofeng Wu, B.E., Wuhan University; M.E., Wuhan University

Chair of Advisory Committee: Dr. Alvin T. Yeh

A detailed understanding of the corneal biomechanical response is an important prerequisite to understanding corneal diseases such as keratoconus and for placing the empirical equations used in refractive surgery on a physical basis. We have assembled a combined nonlinear optical microscopy (NLOM) and optical coherence microscopy (OCM) imaging system to simultaneously capture coregistered volumetric images of corneal morphology and biochemistry. Fudicial markers visible in the OCM volume enabled the calculation of strains for multiple depth layers in rabbit cornea. The results revealed a depth dependent strain distribution, with smaller strains in the anterior stroma and larger strains in the posterior stroma. The stress-strain curves can be grouped readily by depth into three groups: anterior (~20%), transitional mid (~40%), and posterior (~40%). Cross-sectional images of collagen lamellae, visible in NLOM, showed inhomogeneous collagen structure and its response to intraocular pressure along the anterior-posterior direction. The inhomogeneities correlate well with the noted heterogeneous corneal mechanical properties. The combined NLOM-OCM system can

measure corneal microstructure and mechanical response uniquely, thus providing a microstructural understanding of corneal response to changes of collagen structure.

ACKNOWLEDGEMENTS

I would like to thank my advisor Dr. Alvin T. Yeh for his support and guidance through my time in tissue microscopy lab. His extensive knowledge and remarkable insight helped me solved a lot of problems in this study. He also spent a lot of time on improving my skills on presentations and writing papers. I would also like to thank my committee members, Dr. Jay D. Humphrey, Dr. Brian E. Applegate, Dr. Gheorghe Stoica, for their invaluable advice throughout the course of this research.

Thanks also go to my friends and colleagues at Texas A&M University. The lab members in tissue microscopy lab helped me a lot through my research. I would like to thank Adam Larson for setting up the NLOM system, Po-feng Lee for providing the cell-matrix sample in this study, and Anthony Lee for the LabVIEW code of the NLOM system. I would also like to thank Bethany Wicker, Hallie Hutchens, Samantha Steelman, and Xueyi Xie for providing all the rabbit eyes in this study and Zuyi Huang for his great advice on image processing.

Finally, thanks to my mother and father for their encouragement and to my wife for her patience and love.

TABLE OF CONTENTS

CHAPTER Page

CHAPTER Page

LIST OF FIGURES

FIGURE Page

CHAPTER I

INTRODUCTION

Cornea serves as both a physical and chemical barrier and the primary refractive element of the eye. With an avascular structure cornea gets oxygen it needs from the atmosphere via its anterior surface and nutrition from the aqueous humor via its posterior surface. Cornea mechanical strength comes from the collagen lamellae within corneal stroma. Previous studies have shown that both cornea mechanical properties and collagen structure are not homogeneous. Understanding the mechanical properties of cornea and their relationship with collagen structure within the corneal stroma will help to predict the cornea response to changes of cornea tissue from procedures like laser refractive surgeries and wound healing.

1.1 Motivation

There are two problems we want to solve in this study. First, previous studies have shown that it is very difficult to measure cornea mechanical properties layer by layer without damaging the tissue. Second, it has been shown that collagen structure mainly determines cornea mechanical properties. But all the previous studies of cornea mechanical properties and collagen structures were done separately. Until now there was

---

This dissertation follows the style of *Investigative Ophthalmology and Visual Science*.

no method that can simultaneously measure both. So in this study we want to measure the microstructural and mechanical response of rabbit cornea to the change of intraocular pressure (IOP) as a function of depth simultaneously without disturbing the cornea tissue.

To measure cornea mechanical properties layer by layer, we want to use keratocyte nuclei within corneal stroma as markers. By tracing the displacement of the keratocyte nuclei with changes of IOP, the cornea strains at any depth can be calculated. In this study, we built a Fourier domain optical coherence microscopy (OCM) system based on a Kerr-lens mode-locked sub-10-femtosecond (fs) Titanium:Sapphire laser to image keratocyte nuclei in corneal stroma and demonstrated the methodology using OCM to measure cornea strains layer by layer. Using second harmonic generation (SHG) from nonlinear optical microscopy (NLOM), we imaged 3D collagen lamellae structure within corneal stroma and its response to the changes of IOP without any sample preparation like fixing, sectioning, or staining. By combining these two systems, we can simultaneously measure and correlate both collagen structure and mechanical properties of cornea. Thus this method can provide a microstructural understanding of cornea response and may lead to more well-informed algorithms for laser refractive surgeries and measures of glaucoma risk.

1.2 Cornea mechanics

The most common method to measure cornea mechanical properties in intact cornea is with the use of fiducial markers on cornea surfaces to track their movements with the changes in IOP, as illustrated in Figure 1.1. The mechanical properties of cornea can be

calculated using the displacement of these markers. For example, the nonlinear stress-strain relationship has been measured in human and rabbit corneas using the displacement of two mercury drops on the corneal surface. [1] The strains of rabbit cornea

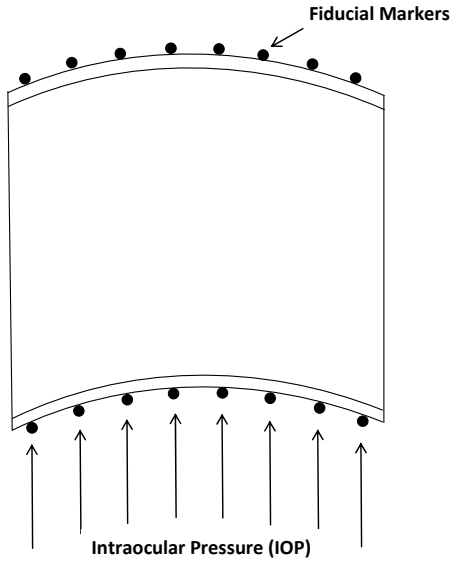

FIGURE 1.1 Measurement of cornea mechanics in intact cornea.

were large at low stress condition. But beyond 20 cm H_2O there was very little stretching of the tissue. While for human cornea there was a smaller compliant region at low pressure condition and then the tissue stretched very little. Shin et al [2] showed nonuniform meridional strain distribution of human cornea by tracking small, self-adherent particles placed on cornea anterior surfaces. Using digital measures of distances between mercury droplet markers fixed on the corneal surfaces, Hjortdal measured both meridional and circumferential mechanical strains of the epi- and endothelial side of human cornea at centre, para-centre, the periphery, and the limbus. [3] The results showed

that in the meridional direction, cornea is stiffer in the centre and para-centre than the periphery and limbus. While in the circumferential direction, cornea is stiffer in the limbus.

However by using surface fiducial markers only the mechanical properties at the corneal surface layer can be measured. There were few studies measuring cornea mechanics at different depth by physically altering the tissue. In one study the cornea was split into stripes and the mechanics of each strip from different depth was measured.[4] They found that the force required to tear apart the strips of rabbit corneal stroma was depth independent. In another study, nonpenetrating central trephine incisions at different depth were made in rabbit eyes to determine the stress-bearing layers in cornea. [5] Their results indicated that the intraocular tension is probably distributed along all the layers in the cornea stroma rather than in certain layers. However, since in these studies the tissue structure in the cornea was changed, some artifacts might be introduced in their results of cornea mechanical properties.

Recently, several new techniques have been used to measure cornea strains depth profile without disturbing the cornea. Ultrasound elasticity microscope was used to produce strain images throughout the cornea depth. [6] They observed a variation of strain with depth in corneal stroma. In a novel application of confocal microscopy, light scattering from cell nuclei was used to image their movement as a function of IOP and calculated strains from anterior and posterior cornea for normally hydrated and swollen corneas and showed higher strains in posterior than anterior stroma and in swollen than

normally hydrated corneal stroma. [7] But until now there has been no study measuring cornea strains layer by layer without damaging the tissue.

It has been believed that collagen lamellae in corneal stroma mainly determine cornea mechanical properties. This was demonstrated by mechanical tests of rabbit and human corneas that showed their stress-strain curves followed that of the stroma rather than that of Descemet's membrane. [1] The correlation between collagen lamellae structure in corneal stroma and cornea mechanical properties also supported this relationship. For example, synchrotron X-ray scattering results from human cornea showed collagen is aligned orthogonally within the center and circumferentially in the periphery and edge. [8] Correspondingly in the meridional direction the cornea is stiffer in the centre, while in the circumferential direction, cornea is stiffer in the limbus. [3] In the anterior-posterior direction, collagen lamellae have an interwoven structure in the anterior stroma and an orthogonal structure in the posterior stroma. [9, 10] But how this depth dependent collagen structure is related to the mechanical properties at different depth has not been studied yet.

1.3 Clinical application of cornea mechanics

Cornea mechanics mainly determines cornea shape and how this shape changes in some procedures like laser refractive surgeries. Thus understanding the correlation between cornea mechanics and microstructure can help predict how cornea tissue will respond to changes of structure.

Cornea is the main refractive power of the eye and the lens behind the cornea provides most of the remaining power and the accommodation capability. In the normal case, light is focused to the fovea of the retina. If light is focused in front of the retina, the eye is called near-sighted, or myopic. If light is focused beyond the retina, the eye is called far-sighted, or hyperopic. When the cornea has different curvatures in the vertical and horizontal meridians, light will not be focused into a single point which is called astigmatism. If the lens cannot provide the accommodation capability anymore, the eye is called presbyopic. Laser refractive surgeries can treat these refractive errors by removing part of the corneal stroma tissue.

Photorefractive keratectomy (PRK) and laser in situ keratomileuis (LASIK) are the most popular laser refractive surgery techniques today. PRK was first performed in human cornea by McDonald et al[11] in 1989. During PRK the corneal epithelium was removed and discarded, an excimer laser is then used to precisely remove the cornea tissue in the stroma. The disadvantage of PRK is that since part of the epithelial layer was discarded, it takes a long time (about 3 days) to regenerate the central epithelial defect and is uncomfortable for the patients and can cause infection. LASIK was first performed by Pallikaris et al[12] in 1991 on human cornea. During LASIK a hinged flap of the stroma with a thickness of 120-180 μm, which consists of epithelium, Bowman's layer, and anterior stroma, is cut either mechanically using a microkeratome or optically using a femtosecond laser and then lifted. An excimer laser is then used to treat the cornea tissue and the flap is repositioned after the treatment. Compared to PRK, LASIK has the advantages of minimum discomfort and fast recovery for the patients after

surgery. However studies have shown that the flap created during LASIK disrupts the interwoven lamellae structure of the anterior stroma, which is the stiffest part of the stroma, and therefore weakens the biomechanical properties of the cornea after the surgery.[13, 14] Recently several new techniques have been developed. In laser-assisted subepithelial keratectomy (LASEK) [15] and epipolis laser in situ keratomileusis (epi-LASIK) [16] a flap is created at the epithelial layer which avoids the stromal flap complications.

Due to incomplete understanding of cornea tissue response to structural changes following ablation, laser refractive surgeries are based on empirical experience and treat cornea as a piece of plastic. [13] Thus all the algorithms used in these laser refractive surgeries are optimized for ensemble averaged responses and cannot predict the result for each individual case. Recently more and more evidence has shown that cornea is not mechanically homogeneous and therefore cornea mechanics need to be considered in the laser refractive surgeries procedures in order to achieve better post-operative results. The cornea responses to the surgeries are mainly determined by stroma. The mechanical properties of the stroma can affect the cornea shape changes after surgeries. Several studies have measured the cornea curvature changes after ablated tissue in central corneal stroma at different depth and observed a depth dependent flattening response after the surgeries. [17-19] This depth dependent response most likely comes from the inhomogeneous properties within the cornea.

1.4 Outline

In the following, the development of the integrated nonlinear optical microscopy (NLOM) – optical coherence microscopy (OCM) system based on a Kerr-lens mode-locked sub-10-fs Titanium:Sapphire laser is described in Chapter II. The combined NLOM-OCM system was then used to image rabbit cornea anatomy and swelling process, which is described in Chapter III. Chapters IV and V describe how the combined NLOM-OCM measured cornea microstructural and mechanical response as a function of depth. Finally in Chapter VI the conclusions of this study and future work are discussed.

CHAPTER II

COMBINED NONLINEAR OPTICAL MICROSCOPY - OPTICAL COHERENCE MICROSCOPY USING SUB-10-FEMTOSECOND PULSES

2.1 Introduction

Different optical microscopy techniques, like nonlinear optical microscopy (NLOM), optical coherence microscopy (OCM), and confocal microscopy, have been widely used in biomedical research with the advantages of non-invasive, high speed, and high resolution imaging of structural and biological information of the sample. Combination of different imaging modalities can provide complementary information of the sample. In this study, we developed a combined NLOM-OCM system based on a Kerr-lens mode-locked sub-10-fs Titanium:Sapphire laser to simultaneously image different components of the sample.

2.1.1 Kerr-lens mode-locked sub-10-femtosecond laser

The first laser was invented by Theodore H. Maiman[20] in 1960 and since then it has been widely used in biological research as the light source. Laser normally contains the gain medium, the pump energy for the gain medium, and highly reflective optical cavity. The pump energy, which is commonly either optical or electrical, excites some electrons in the gain medium from the ground to excited state. The generation of laser requires that the population of electrons in the excited states is more than that in the lower-energy states, which is called population inversion. While the electrons are in the excited states, they can relax to the lower-energy states by spontaneous emission, stimulated emission,

or non-radiative relaxation like heat. The amplification effect in laser generation requires that stimulated emission, which was first described by Albert Einstein[21] in 1917, dominates the emission process. During stimulated emission the electrons in the excited states interact with a photon having the correct energy, relax to the ground state, and produce another photon with the same phase, frequency, polarization, and travel direction as the original photon. If the generated photons are reflected and transverse the gain medium repeatedly, a cascade effect is produced. The laser used in this study employed a frequency-doubled Nd:YVO_4 solid-state laser as a pumping source to excite the gain medium Ti:Al_2O_3 crystal.

To extract the laser out of the cavity, one end of the cavity is partially transparent. To maintain the resonance condition for standing waves, the cavity length needs to satisfy the following condition:

$$\upsilon = \frac{nc}{2L} \tag{2.1}$$

where υ is the resonate frequency, n is an integer, c is the light speed, and L is the cavity length. This means that resonate frequency depends on cavity length. Normally the laser cavity length allows many resonate frequencies (or modes) to exist and which frequencies are actually observed depend on which frequencies have a gain higher than the threshold. This threshold depends on loss in the cavity due to, for example, scattering, absorption, and output loss.

The output of the laser can be either continuous wave (CW) or pulse. In CW mode, the output of the laser is relatively constant over time. In pulse mode, the output of laser varies with time. The different frequencies in the laser cavity have random phases and

can interfere with each other both constructively and destructively. In a laser with many frequencies of random phases, this interference will average the output intensity. If the phases of cavity frequencies are fixed, these frequencies can (constructively) interfere and generate pulses.

Mode-locking is a technique that introduces a fixed phase relationship between different modes. Mode-locking methods can be divided into two categories: active and passive. Active mode-locking uses an electro-optic component in the laser cavity to lock the phases of different modes by introducing a phase modulation to the existing laser modes. In passive mode-locking no external component is required and the laser light can cause some change in the cavity which then can change the laser light itself. In our laser a passive mode-locking technique called Kerr-lens mode-locking (KLM) is used to generate pulses.

KLM uses a nonlinear optical effect called optical Kerr effect, in which the optical medium responds nonlinearly to the external electric field. If the laser light has very high intensity, it can change the refractive index (n) of the gain medium as follows:

$$n(I) = n_0 + n_2 I \tag{2.2}$$

where n_0 is a linear refractive index, n_2 is material dependent second-order nonlinear portion of the refractive index, I is the laser light intensity. Thus an intense laser light can generate an intensity dependent refractive index within the gain medium. The laser light intensity has a non-uniform Gaussian profile, which will produce a gradient index lens within the gain medium and cause the laser beam to self-focus. Thus the short bursts of light (pulses) will be focused differently than CW light. Then an aperture can be used

to block the CW light. This aperture can be either a hard aperture, for example a pinhole or slit, or a soft aperture, in which the pumped region of the gain medium is overlapped with the pulse beam. In our laser, KLM induces loss in CW light by detuning a focusing mirror relative to the gain medium and second focusing mirror in a near confocal resonator cavity. As the pulsed beam has a smaller diameter than the CW beam, the focus of the pump beam will overlap more tightly with the pulsed beam than CW beam, which increases the gain efficiency for the pulsed beam when the resonator is in stable operation. Figure 2.1 shows a schematic of this process.

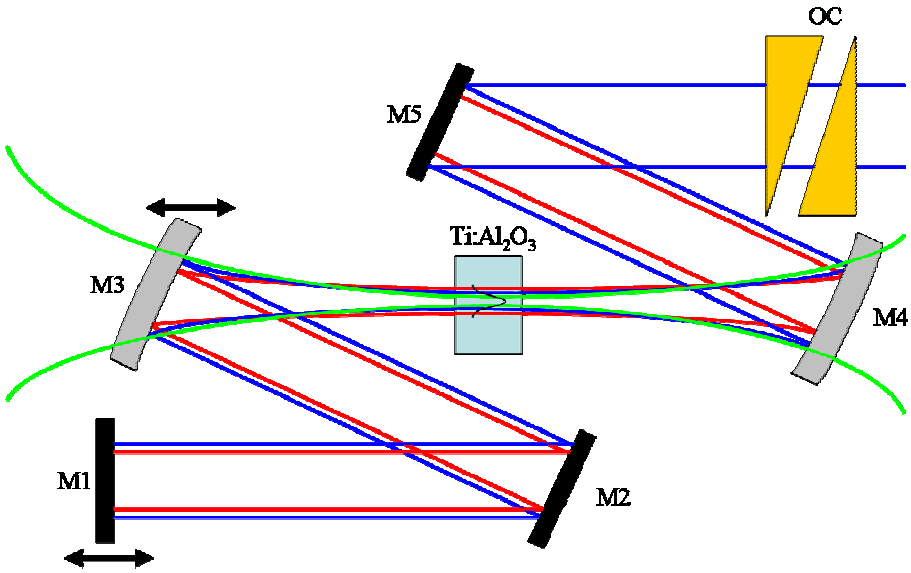

FIGURE 2.1 Soft aperture KLM. The Gaussian curve in the gain medium indicates the intensity dependent refractive index profile induced by the optical Kerr effect. The double headed arrow above M3 indicates the detuning of the curved mirror to favor CW or pulsed operation. Toggling of M1 will induce modelocking. Green: Pump beam. Red: CW beam. Blue: Pulsed beam. M1: End mirror. M2 & M5: Intracavity mirrors. M3 & M4: Curved mirrors. OC: Output coupler.

Since the pulse duration is the Fourier transform of the pulse spectrum, the more resonate frequencies in the pulse, the shorter duration the pulse. Thus the laser gain medium must have a broad gain profile. The gain medium Ti:Al_2O_3 used in this laser has a very broad gain cross-section. [22] Self-phase modulation (SPM) effect further increases the pulse spectrum in our laser. SPM is also a nonlinear optical effect. The refractive index change in the optical Kerr effect described previously will produce a phase shift in the pulse which will change the pulse's frequency spectrum. Assuming a Gaussian pulse with the following form:

$$I(t) = I_o \exp\left(-\frac{t^2}{\tau_0^{\,2}}\right) \tag{2.3}$$

where I_0 is the peak intensity, τ_0 is the FWHM of the pulse duration. The phase change from the refractive index change can be written as

$$\phi(t) = \omega_o t - \frac{2\pi}{\lambda_0} Ln(I) \tag{2.4}$$

where L is the propagation length through the medium, ω_o is the central frequency of the pulse. The frequency shift from the phase shift can be described as

$$\omega(t) = \frac{d\phi(t)}{dt} = \omega_0 - \frac{2\pi L}{\lambda_0}\frac{dn(I)}{dt} \tag{2.5}$$

Substituting the Equation 2.2 and 2.3 into Equation 2.5

$$\omega(t) = \frac{d\phi(t)}{dt} = \omega_0 - \frac{2\pi L}{\lambda_0}\left(n_2 I_0 \frac{-2t}{\tau_0^2}\exp\left(-\frac{t^2}{\tau_0^2}\right)\right) = \omega_0 + \frac{4\pi L n_2 I_0 t}{\lambda_0 \tau_0^2}\exp\left(-\frac{t^2}{\tau_0^2}\right) \tag{2.6}$$

Thus if n_2 is positive from normal dispersion, the leading edge of the pulse will be shifted to lower frequencies and the trailing edge of the pulse will be shifted to higher

frequencies and the spectrum of the pulse is broadened. The linear chirp associated with this instant frequency shift is

$$\alpha = \frac{d\omega(t)}{dt}\Big|_0 = \frac{4\pi L n_2 I_0}{\lambda_0 \tau_0^2} \tag{2.7}$$

To reduce the pulse duration of the laser, the positive frequency chirp induced by SPM must be counteracted with negative group-velocity dispersion (GVD). The pulses in our laser have a broad spectrum with 133 nm full-width-half-maximum (FWHM).

2.1.2 Nonlinear optical microscopy

Nonlinear optical microscopy (NLOM) uses the nonlinear signals from the sample normally generated by femtosecond laser pulses to provide 3-dimentional (3D) imaging of thick biological tissue and live animals. The most common nonlinear signals used in biomedical research are multi-photon excited fluorescence (including two-photon and three-photon), second- and third- harmonic generation (SHG, THG), and coherent anti-Stokes Raman scattering (CARS). Nonlinear polarization P of a sample can be described by the Taylor expansion of the n^{th} order susceptibility of the sample, $\chi^{(n)}$, and the electric field, E,

$$P = \chi^{(1)} \otimes E + \chi^{(2)} \otimes E \otimes E + \chi^{(3)} \otimes E \otimes E \otimes E + \ldots \tag{2.8}$$

in which $\chi^{(1)}$ corresponds to 1^{st}-order processes like absorption and reflection, $\chi^{(2)}$ corresponds to 2^{nd}-order processes like SHG and sum and difference frequency generation, $\chi^{(3)}$ corresponds to 3^{rd}-order processes like multiphoton absorption, THG, and CARS. Two-photon excited fluorescence (TPEF) and SHG can be implemented on

the same setup and were used in our NLOM system to simultaneously image both the cells and collagen structure in the cornea, respectively.

2.1.2.1 Second harmonic generation

Second harmonic generation (SHG) was one of the earliest nonlinear optical processes discovered by Franken et al[23] in 1961. The first SHG in biological sample was demonstrated by Freund et al[24] in 1986. In this process, the light at frequency ω incident on a nonlinear optical material creates light at frequency 2ω, as illustrated in Figure 2.2 (a). The energy-level diagram of this process can be visualized in Figure 2.2 (b). In contrast to TPEF in which some of the incident light energy is lost during the relaxation of the excited state, SHG is energy conserving and thus the emitting photon is exactly twice the energy (half the wavelength) of the incident photon. Similar to TPEF, the amplitude of SHG is proportional to the squared intensity of the incident light and thus has the same inherent optical sectioning capability.

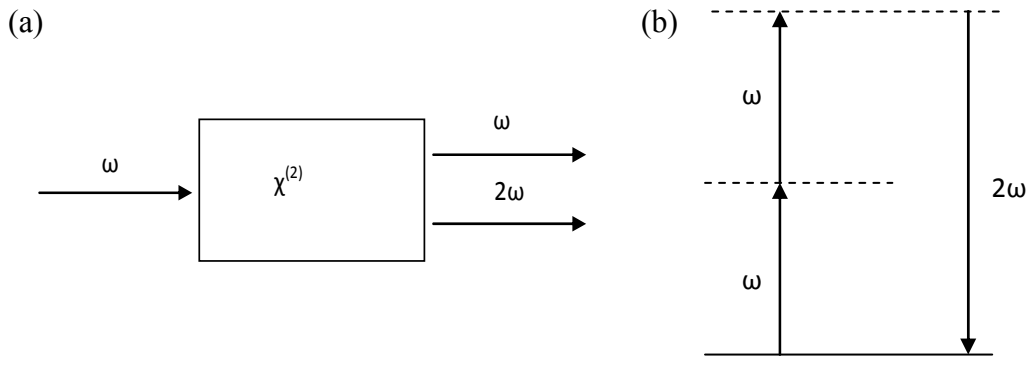

FIGURE 2.2 Second harmonic generation process.

The second-order nonlinear susceptibility ($\chi^{(2)}$) of SHG is related to the molecular hyperpolarizability (β) using the following equation: [25]

$$\chi^{(2)} = N_s \langle \beta \rangle \tag{2.9}$$

where N_s is the molecular density and the brackets denote an orientational average. So only the materials that have noncentrosymmetric structures can generate SHG. For example collagen in biological tissue can generate strong SHG signals due to its triple helix structure and long range molecular order.

The SHG excitation spectrum can be described as[26]

$$T(\omega) = \left| \int_0^\infty E\left(\frac{\omega}{2} + \Omega\right) E\left(\frac{\omega}{2} - \Omega\right) d\Omega \right|^2 \tag{2.10}$$

where $E(\omega)$ is the pulse electric field in the frequency domain, Ω is an iterative variable that ensures integration over all possible combinations of frequency components such that $\omega = \omega_a + \omega_b$. Since SHG does not depend on frequency, the transition probability of SHG intensity can be calculated as

$$\Gamma \propto \int_0^\infty \gamma T(\omega_0) d\omega_0 = \int_0^\infty \gamma \left| \int_0^\infty E\left(\frac{\omega_0}{2} + \Omega\right) E\left(\frac{\omega_0}{2} - \Omega\right) d\Omega \right|^2 d\omega_0 \tag{2.11}$$

where γ is a frequency-invariant response function. Assuming Gaussian pulses with center wavelength at 800 nm, logarithmic plot of the transition probability of SHG intensity as a function of pulse duration is shown in Figure 2.3. It shows that the transition probability of SHG intensity decreases with the increase of pulse duration in time.

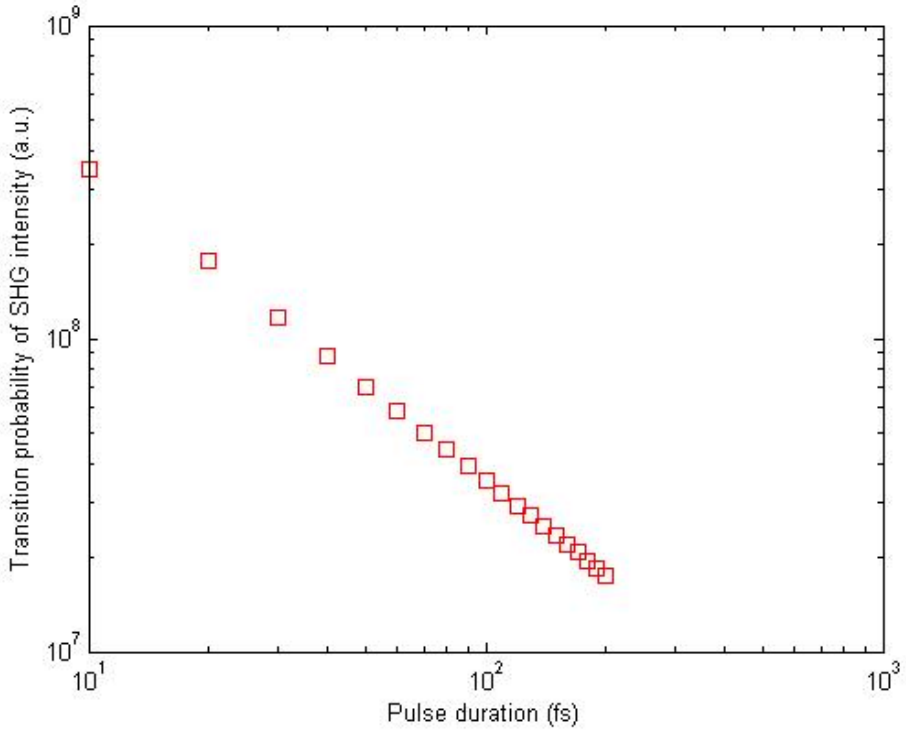

FIGURE 2.3 Logarithmic plot of transition probability of SHG intensity as a function of pulse duration.

SHG has several advantages in biomedical imaging. Since there is no excitation of molecules in this process, there is no photo-bleaching or photo-toxicity from the sample, which is a problem in TPEF. Also since SHG is normally generated from the intrinsic structure of the sample, there is no need to label the sample with exogenous probes. In SHG imaging, near-infrared light is normally used, which can increase the penetration depth in biological tissue. Since SHG is a coherent process, the SHG signals have well-defined polarizations and can be used to determine the orientation of the structure in the tissue.

The resolutions of both TPEF and SHG microscopy are determined by the focusing objectives used in the microscope setup. Their transverse resolutions Δx can be estimated by

$$\Delta x = \frac{4\lambda_0}{\pi} \cdot \frac{f}{d} \tag{2.12}$$

where λ_0 is the central wavelength of the laser source, f is the focal length of the objective, d is the beam diameter on the objective. The axial resolutions can be estimated by the confocal parameter (or depth of focus, b) of the objectives:

$$b = 2z_R = \frac{2\pi\omega_0^2}{\lambda_0} \tag{2.13}$$

where z_R is the Rayleigh range, ω_0 is the minimum beam waist of the Gaussian beam.

2.1.2.2 Two-photon excited fluorescence

Two-photon process was first predicted by Maria Göppert-Mayer[27] in 1931 in her doctoral dissertation. This process requires that the two photons interact with the molecule simultaneously, which makes it dependent on the squared intensity of the incident light. Figure 2.4 showed the two-photon excitation process in which two incident photons induce the electronic transition from the ground state to the excited state via virtual state. It was not until 1961 with the invention of high-peak-power lasers that the two-photon absorption was first demonstrated. [28] The first two-photon excited fluorescence (TPEF) microscopy was demonstrated by Denk et al[29] in 1990 using a colliding-pulse, mode-locked (CPM) dye laser with a pulse duration of 100 fs and central wavelength at 630 nm. Since then TPEF has been widely used in biomedical

research, together with the rapid development of new fluorescence probes and ultrafast laser technology. Now two-photon microscopy has become a popular technology in fluorescence imaging of biological thick tissue and live animals.

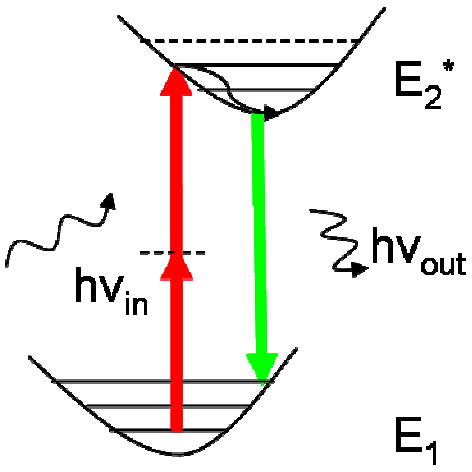

FIGURE 2.4 Two-photon excitation process.

The two-photon excitation spectrum of the pulse can also be described using Equation 2.10 for SHG. In contrast to SHG, the two-photon transition probability depends also on the two-photon absorption spectrum of the fluorophores. [30] Thus the two-photon transition probability can be described as the overlap between two-photon excitation spectrum of the pulse and the two-photon absorption spectrum of the fluorophores using the following equation:[31]

$$\Gamma \propto \int_0^\infty \gamma(\omega_0)\left|\int_0^\infty E\left(\frac{\omega_0}{2}+\Omega\right)E\left(\frac{\omega_0}{2}-\Omega\right)d\Omega\right|^2 d\omega_0 \qquad (2.14)$$

where $\gamma(\omega_0)$ is the two-photon absorption spectrum of the fluorophores.

One of the main advantages of two-photon excitation compared to one-photon excitation is that the generated signal is proportional to the squared intensity of the excitation light, which means that only the sample in the focal volume will be excited. So two-photon excitation has the inherent capability of optical sectioning within thick sample and can be used for 3D imaging without the need for confocal pinholes to remove the out-of-focus light. For biological tissue, two-photon excitation generally uses near infrared light, which can penetrate deeper in the tissue. Since only the focal volume is excited, photo-bleaching and photo-damage are greatly reduced for two-photon processes compared to one-photon processes.

Pulsed laser is usually used in two-photon excitation to improve the excitation efficiency while keeping the average power on the sample relatively low. Two-photon excited fluorescence depends on the average squared intensity ($\left\langle I(t)^2 \right\rangle$), which can be calculated using the following equation: [32]

$$\left\langle I(t)^2 \right\rangle = g_p \left\langle I(t) \right\rangle^2 / (R\tau) \tag{2.15}$$

where $\left\langle I(t) \right\rangle^2$ is the squared average intensity, g_p is a unitless factor that depends on the temporal laser pulse shape (0.66 for Gaussian pulses), R is the number of pulses per second, and τ is the full-width half-maximum (FWHM) of the pulse. For 10-fs pulses with repetition rate of 75 MHz, the enhancement of two-photon excitation efficiency compared to CW laser is about 8.8×10^6.

In two-photon excitation, the two incident photons were not necessary be the same wavelength. As long as the wavelengths of the two photons satisfy the following equation, [33] two-photon excitation can be achieved,

$$\frac{1}{\lambda_{ab}} = \frac{1}{\lambda_1} + \frac{1}{\lambda_2} \tag{2.16}$$

where λ_{ab} is the absorption wavelength of the absorber, and λ_1 and λ_2 are the wavelengths of the incident photons. Sub-10-fs pulses in our laser have a broadband spectrum with FWHM of 133 nm, thus multiple fluorescence probes can be excited simultaneously.

2.1.3 Optical coherence microscopy

Optical coherence microscopy (OCM) is an adaptation of a widely used interferometric technique optical coherence tomography (OCT) with the use of high numerical aperture (NA) objective. By combining the coherence gate from OCT and confocal gate from the high NA objective, OCM has enhanced optical sectioning capability in highly scattering biological tissue. [34]

OCT is a recently developed optical imaging technology by Huang et al[35] in 1991 that is analogous to ultrasound B mode imaging. To detect the extremely fast 'echo' time of light, an interferometer is used in OCT. Figure 2.5 shows a simple Michelson interferometer that is most popular in OCT design. The beam from the light source is split by a beam splitter into a reference (E_R) and sample beam (E_S). The reference beam is reflected by a mirror and recombined to interfere with that reflected from the sample at the beam splitter and directed to the detector. The combined beam is the sum of the

electromagnetic fields of the two beams. The detector measures the intensity of the combined beam and can be described as:

$$I_O \sim \left|E_R\right|^2 + \left|E_S\right|^2 + 2E_R E_S \cos(2k(l_R - l_S)) \tag{2.17}$$

where k is the angular wave number, l_R and l_S are the path lengths of reference and sample arm, respectively. $\Delta l = l_R - l_S$ is the path length difference and I_O will oscillate as a function of Δl to form an interference. The envelop of the oscillation can be extracted to resolve the sample reflectivity as the amplitude of the oscillation is proportional to E_S. By scanning the reference mirror axially, depth-resolved E_S (A-line) can be acquired. Transverse scanning is used for cross-sectional image generation.

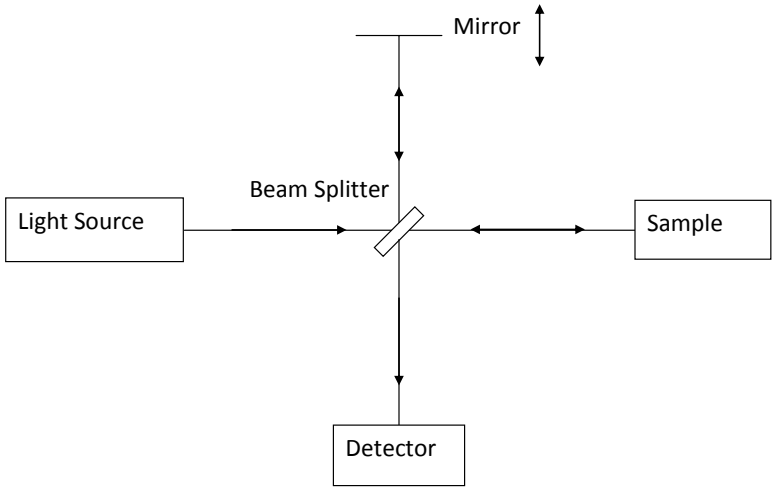

FIGURE 2.5 Schematic of Michelson interferometer.

In OCT normally a low coherence light source (for example, superluminescent diode (SLD)) is used so that the reflected beam from the reference arm and sample arm

will interfere only when the path lengths difference are within the coherence length. The coherence length is the spatial extent in which the electric field is still correlated along its propagation direction and is inversely proportional to the bandwidth of the light source. Thus the axial resolution of OCT is determined by the coherence length of the light source and decoupled from the transverse resolution. For a Gaussian source that is usually used in OCT, the axial resolution Δz is,

$$\Delta z = \frac{2\ln 2}{\pi} \cdot \frac{{\lambda_0}^2}{\Delta\lambda} , \tag{2.18}$$

where λ_0 and $\Delta\lambda$ are central wavelength and the FWHM of the source spectrum, respectively. The axial resolution is inversely proportional to the bandwidth of the light source and thus a broadband light source is needed for high axial resolution. The transverse resolution (Δx) of OCT is determined by the focusing optics of the system and can be calculated as,

$$\Delta x = \frac{4\lambda_0}{\pi} \cdot \frac{f}{d} , \tag{2.19}$$

where f is the focal length of the objective lens and d is the beam diameter on the objective lens. Thus to increase the transverse resolution, a high NA ($NA \approx \frac{d}{2f}$) objective is needed. However, increasing objective NA will decrease the depth of focus (or confocal parameter) z_f . The relation between transverse resolution and depth of focus is,

$$z_f = 2z_R = \frac{\pi \Delta x^2}{2\lambda_0} , \tag{2.20}$$

where z_R is the Rayleigh range. In OCT a low NA objective is normally used for a large depth of field, while in OCM a high NA objective is used for high transverse resolution.

The method described previously is called time-domain OCT (TDOCT). Recently there is a new technique called Fourier-domain OCT (FDOCT) first described by Fercher et al[36] in 1995 which can generate the A-lines without scanning the reference mirror and thus greatly increases imaging speed. In FDOCT, all scatters in an A-line are simultaneously measured and contribute to the interference signal. An A-line image can be acquired by Fourier transform of the spectrum of the interferogram. There are two ways to detect the spectrum. A detector array can be used to detect the whole spectrum, which is dispersed by a diffraction grating, at once, or a single detector can be used to detect the spectrum sequentially with a frequency swept laser source.

As mentioned earlier, OCM combines OCT with high NA objective to increase the transverse resolution at the price of reduced depth of focus. Compared to confocal microscopy, OCM has enhanced optical sectioning capability in highly scattering sample and thus can image deeper in biological tissue by combining the coherence gate from OCT with the confocal gate from the high NA focusing lens. Since a high NA objective is used in OCM, only the signal from the tightly focused spot within the sample can be detected. Thus to generate an image, a 2-dimentional (2D) scan is needed. Similar to OCT, OCM can be achieved in both time-domain and Fourier-domain. In this study we developed a Fourier-domain OCM.

2.2 Methods and materials

2.2.1 NLOM-OCM schematic

In this study a Fourier domain OCM was integrated into an existing custom-built NLOM setup previously described. [37] A schematic of the integrated NLOM-OCM setup is shown in Figure 2.6. Sub-10-fs laser pulses (800nm, FWHM, 133 nm) from a Kerr-lens mode-locked Ti:Al_2O_3 oscillator (Femtosource compact, Femtolasers, Vienna, Austria) pumped by a frequency-doubled Nd:YVO_4 solid-state laser (Verdi, Coherent, Santa Clara, CA) were used as a common source for both NLOM and OCM. After the appropriate number of bounces from a pair of dispersion compensation mirrors (GSM 210, Femtolasers), the beam was split by a 50/50 beam splitter. One beam was directed to the sample for NLOM and as the sample arm of OCM; the other was used as the reference arm of OCM. A pair of prisms and BK7 glass (the thickness of which depends on the objective used in the sample arm) were placed in the reference arm to match dispersion of sample and reference arm in the OCM. The beam in the sample arm was coupled into the epifluorescence port of an upright microscope (Axioskop2 MAT, Carl Zeiss, Thornwood, NY) and directed to the microscope objective (40× Achroplan, 0.8 NA or 63× Achroplan, 0.95 NA, Carl Zeiss) by using a short-pass dichroic mirror (635dcspxruv3p, Chroma, Rockingham, VT). NLOM signals generated from the sample were collected by the focusing objective and directed to a two-channel detector for image rendering at two different wavelengths for SHG (HQ405/40M, Chroma) and two-photon excited fluorescence (HQ525/50M, Chroma). Backscattered laser from the sample was also collected by the focusing objective, reflected back to the beam splitter,

and combined with the return beam from the reference arm. The combined beam was focused into a single mode fiber and directed to a home-built spectrometer. Each pixel in the OCM image was generated by integrating the interferometric signal over the source coherence length at the optical pathlength corresponding to the focal plane. Custom software written on the LabVIEW (National Instruments, Austin, TX) platform acquired NLOM and OCM images simultaneously with frame rate of 0.125 Hz. 2D en face images (256 X 256 pixels) were rendered by raster scanning the laser beam with a pair of galvanometer mirrors and 3D renderings were reconstructed from image stacks acquired using a linear translation stage.

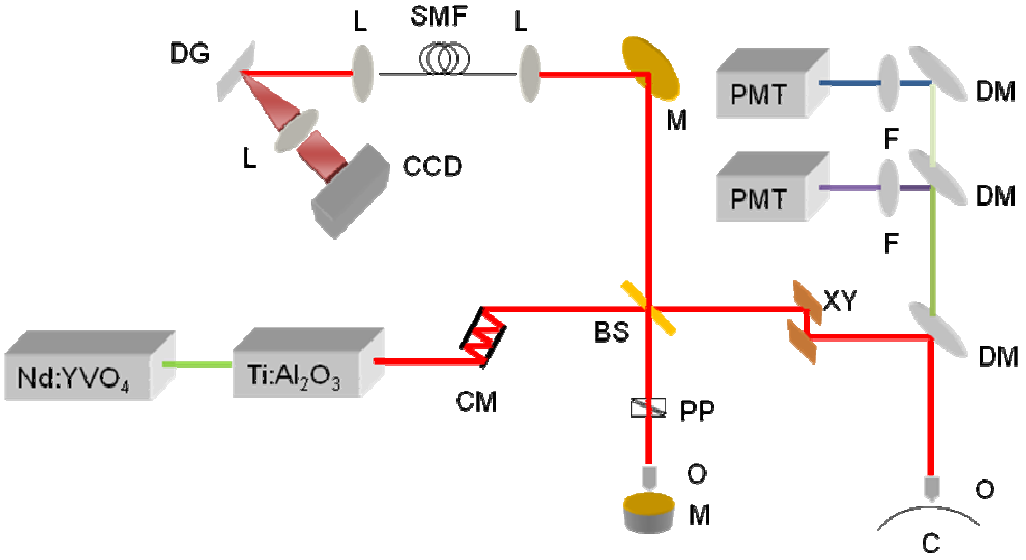

FIGURE 2.6 NLOM-OCM setup. BS, beam splitter; CM, chirp mirror; C, cornea sample; CCD, charge-coupled detector; DG, diffraction grating; DM, dichroic mirror; F, filter; L, lens; M, mirror; O, objective; PMT, photomultiplier tube; SMF, single-mode fiber; XY, XY scanning mirrors.

2.2.2 Spectrometer design and calibration

The OCM in this study used a Fourier domain detection scheme in which a spectrometer was built to detect the spectrum of the OCM signal. To achieve the best result, optical system design software ZEMAX (ZEMAX, Bellevue, WA) was used to simulate the spectrometer design. Figure 2.7 showed the 3D layout of the spectrometer design in ZEMAX simulation.

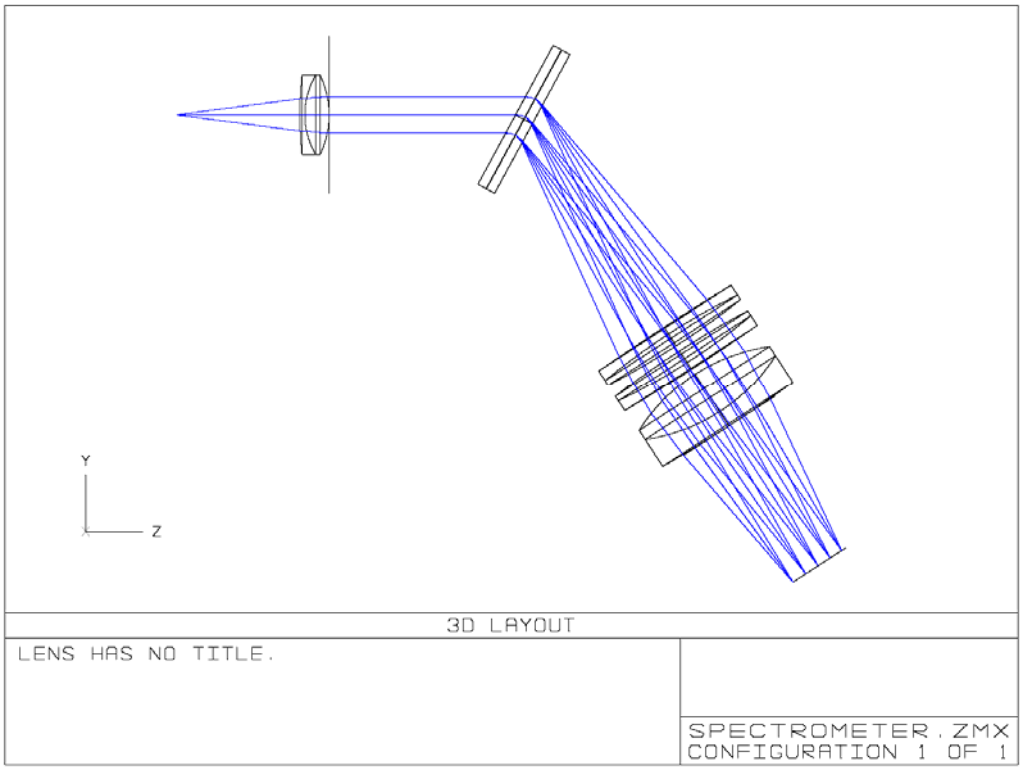

FIGURE 2.7 3D layout of spectrometer design in ZEMAX simulation.

In this simulation, 5 wavelengths (700 nm, 750 nm, 800 nm, 850 nm, and 900 nm) that cover most of the spectrum of our laser were used to simulate the whole spectrum of the laser source. The light coming out of the single mode fiber is simulated as a point source with 0.13 NA aperture, which is same as the NA of the fiber. The beam is then collimated using an achromat and dispersed by a diffraction grating. In this simulation a transmission grating was used, while in the experiment a reflective diffraction grating (NT43-211, Edmund Optics, Barrington, NJ) was used. However this should not affect the results as the dispersion capability of a grating is only determined by the groove number, beam size on the grating, and the incident angle of the beam. A triple lens design was used to focus the dispersed spectrum of the beam onto a 2048-pixel line scan camera (L104k-2k, Basler, Exton, PA).

Since the camera we used has a pixel size of 10 μm by 10 μm with a total of 2048 pixels, for best use of the CCD sensor, the whole spectrum needs to be focused to about 20 mm in length. The spot diagram from ZEMAX in Figure 2.8 showed that for the spectrum range 700 – 900 nm the focused length is 19 mm, which is very close to the sensor size. To make sure there is no cross-talk at adjacent pixels on the CCD sensor, the Huygens PSF cross-section at the focus was calculated. Figure 2.9 showed that the FWHM of the Huygens PSF cross-section is about 10 μm, close to the pixel size.

The spectrometer was calibrated after setup. An argon lamp (6030, Oriel, Stratford, CT) with known spectrum was used as the calibration light source and put in front of the incident fiber of the spectrometer. The spectrum of the argon lamp was detected by the spectrometer, as shown in Figure 2.10 with x axis as the pixel number and y axis as the

intensity. The pixel position (n) of each peak in the spectrum was found and correlated to the wavelength (λ) of that peak according to the standard spectrum of the argon lamp. A third-order fit was then used to fit wavelength (λ) of the spectrum to the pixel position (n) of the CCD sensor, as shown in Figure 2.11.

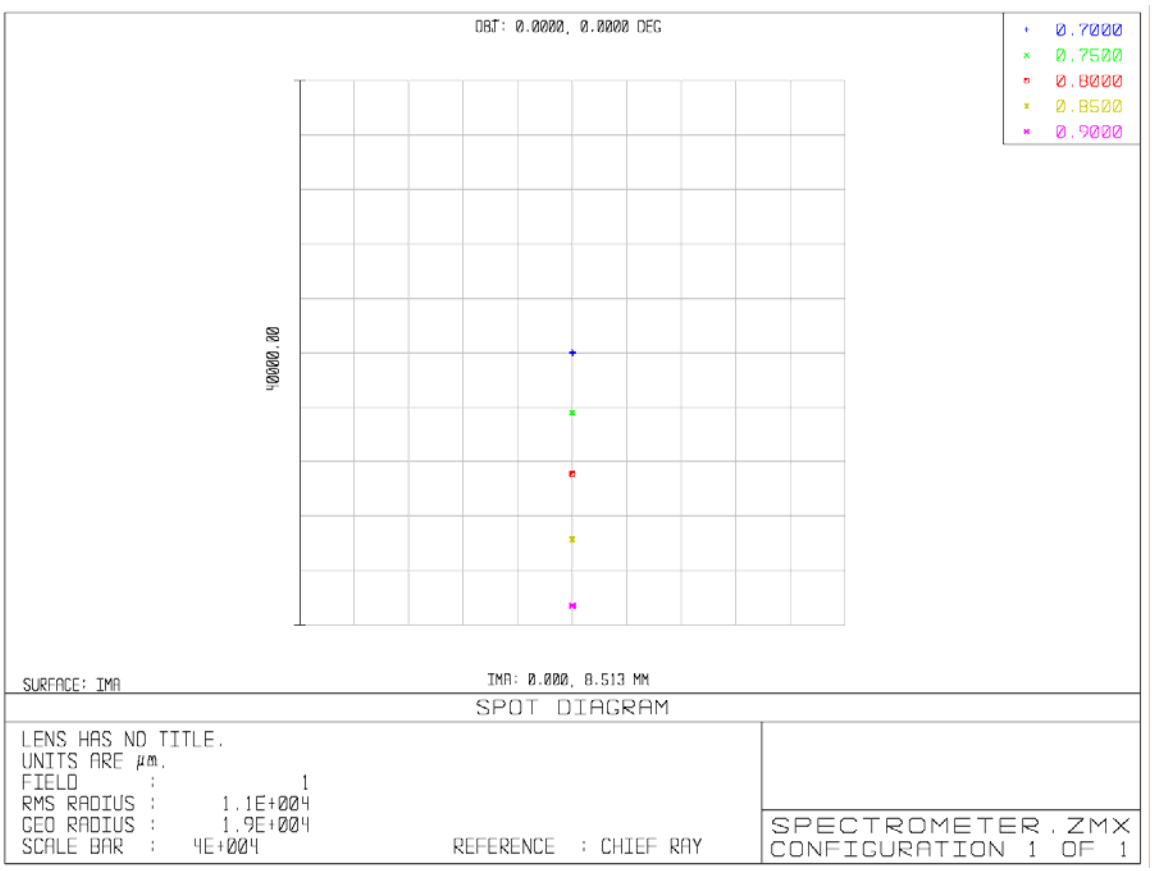

FIGURE 2.8 Spot diagram at focal point in ZEMAX simulation.

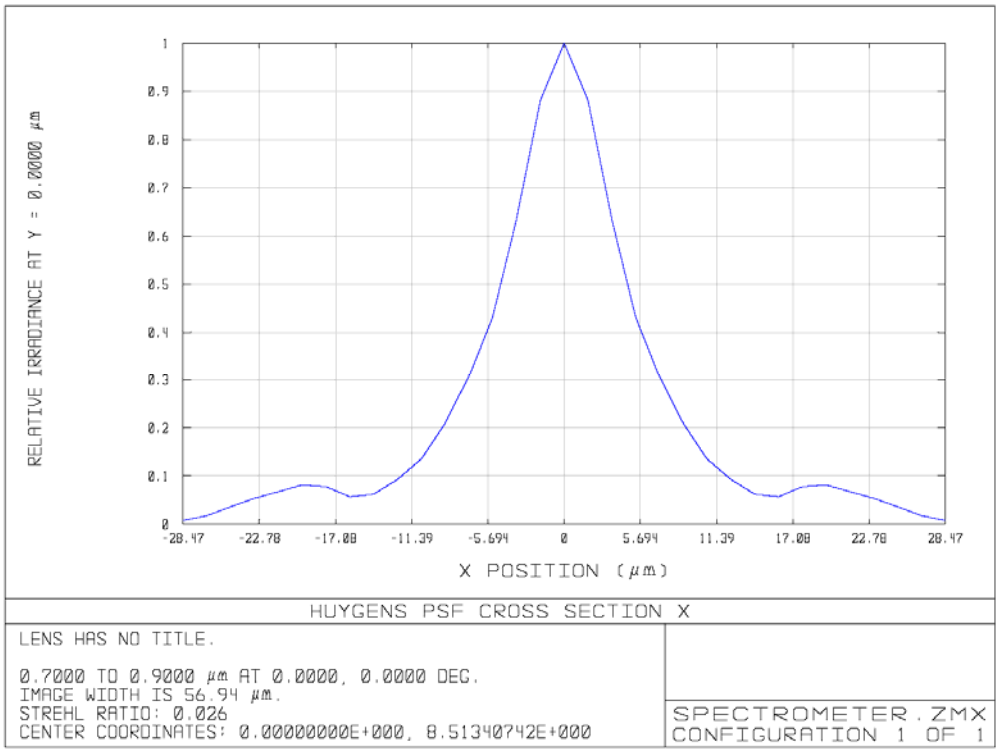

FIGURE 2.9 Huygens PSF cross section at focal point in ZEMAX simulation.

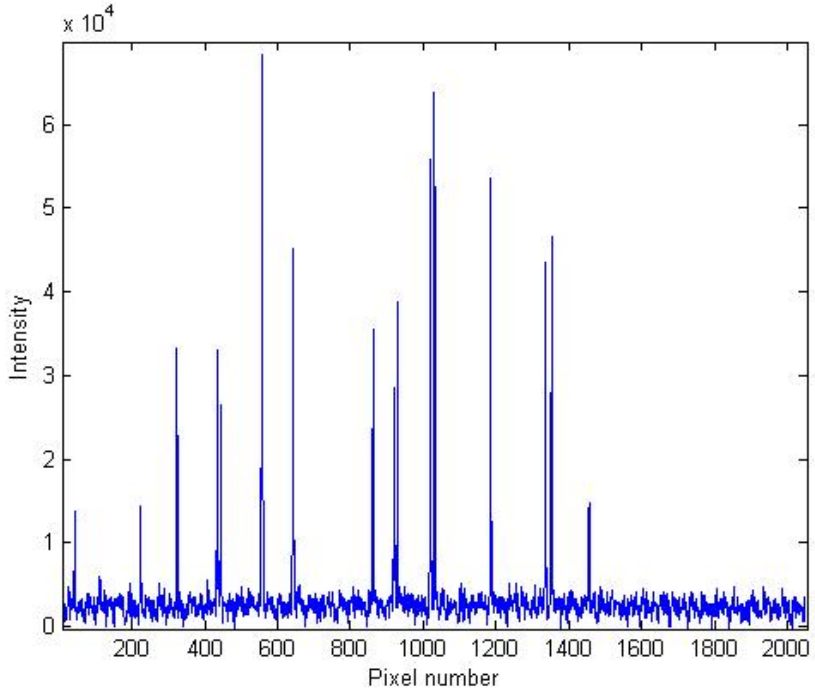

FIGURE 2.10 Spectrum of the argon lamp detected by the spectrometer.

2.3 Results

2.3.1 Axial resolution of OCM

Theoretically the axial resolution of OCM depends on a combination of confocal and coherence gate. The best axial resolution is achieved when the confocal and coherence gate are overlapped. The axial PSF of OCM decreases exponentially from the focus plane rather than geometrically as in confocal microscopy. Thus near the focus the axial resolution of OCM is dominated by the confocal gate, while far from the focus the coherence gate will strongly reject the scattered light. In our OCM setup, the coherence

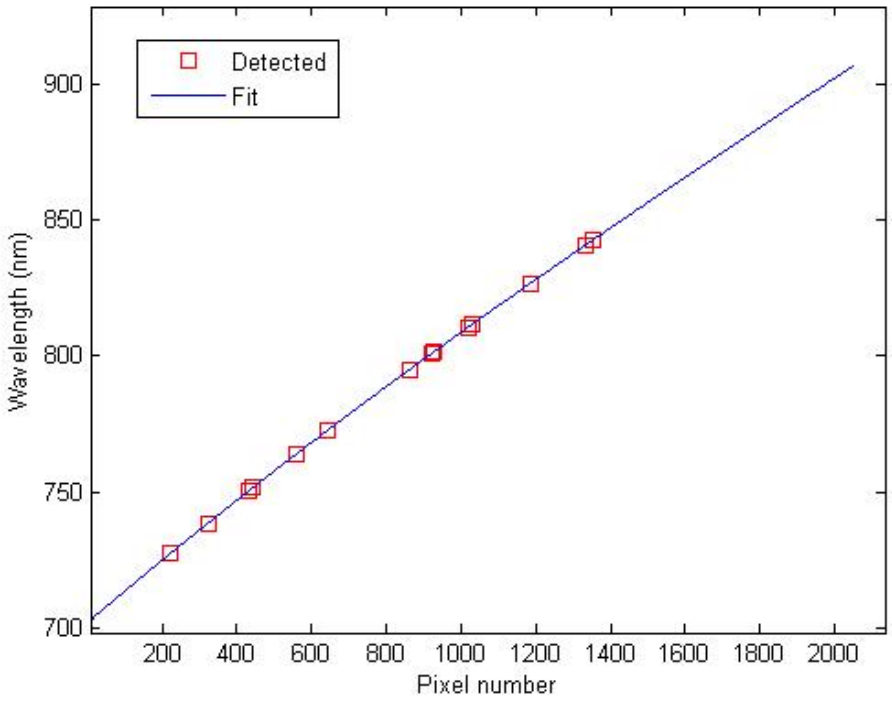

FIGURE 2.11 Third-order fit of wavelength of the argon lamp spectrum to the pixel position of the CCD sensor.

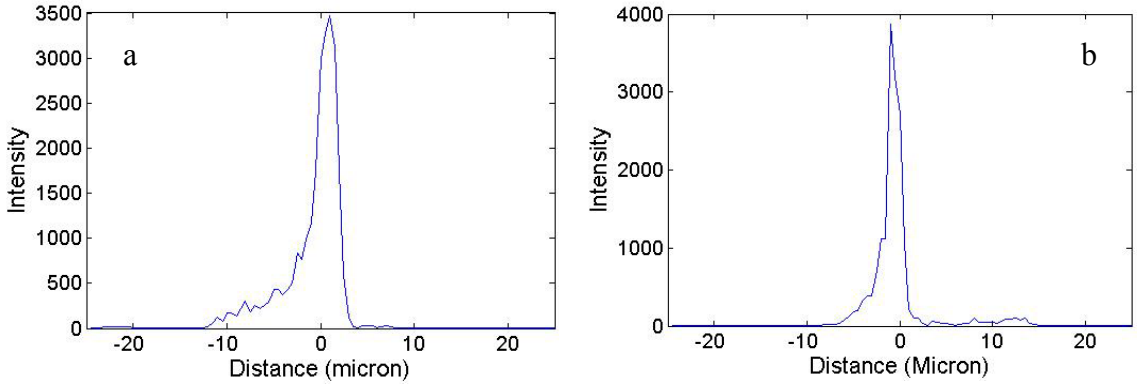

FIGURE 2.12 Measured axial resolution of OCM. a, 40x objective; b, 63x objective.

gate is 2.1 μm and the confocal gates are about 1.9 μm and 1.4 μm for the 40x and 63x objectives, respectively.

The actual axial resolution of the OCM was measured by taking the OCM signal with a mirror moving across the focus of the objective with 0.5 μm step size. In this study both 40x (0.8 NA) and 63x (0.95 NA) objectives were used and their axial resolution were measured, as shown in Figure 2.12. The axial resolutions of 40x and 63x objectives measured were 2 μm and 1.5 μm, respectively. These measured axial resolutions were very close to the theoretical values.

2.3.2 Signal-to-noise ratio of OCM

The signal-to-noise ratio (SNR) for OCT/OCM can be defined as

$$SNR = 10 \times \log_{10} \frac{QP_s \Delta t}{h\upsilon} \tag{2.21}$$

where Q is the quantum efficiency of the detector, P_s is the laser power on the sample, Δt is the integration time of the detector, $h\upsilon$ is the photon energy. Given 10 mW power

on the sample, 122 μs integration time for the line scan camera and assuming the camera quantum efficiency of 0.5, the theoretical SNR of the OCM can be calculated as 124 dB.

Maximum SNR is normally achieved when limited by shot noise. The SNR of our OCM system was measured using a gold mirror as the sample. An OD 2.0 neutral density filter was put in the sample arm to simulate attenuation in the real sample and a combination of OD 1.3 neutral density filters were put in the reference arm to set the OCM in shot noise detection. The laser power on the sample and the integration time of the camera were set according to the values used in the previous calculation of the theoretical SNR. SNR was obtained by first taking about 300 PSFs (a) of the OCM signals followed by taking another about 300 PSFs (b) with the sample arm blocked. The averages of these two PSFs are shown in Figure 2.13. The SNR was calculated to be 110 dB by dividing the maximum of the PSF of the OCM signal (a) with the standard deviation of PSF (b) at the position corresponding to the peak area in PSF (a). This measured SNR is a little lower than the theoretical SNR. This loss of SNR is probably due to some loss in the system setup, for example the loss in coupling the beam into the single mode fiber, the loss at diffraction grating and the other optical components.

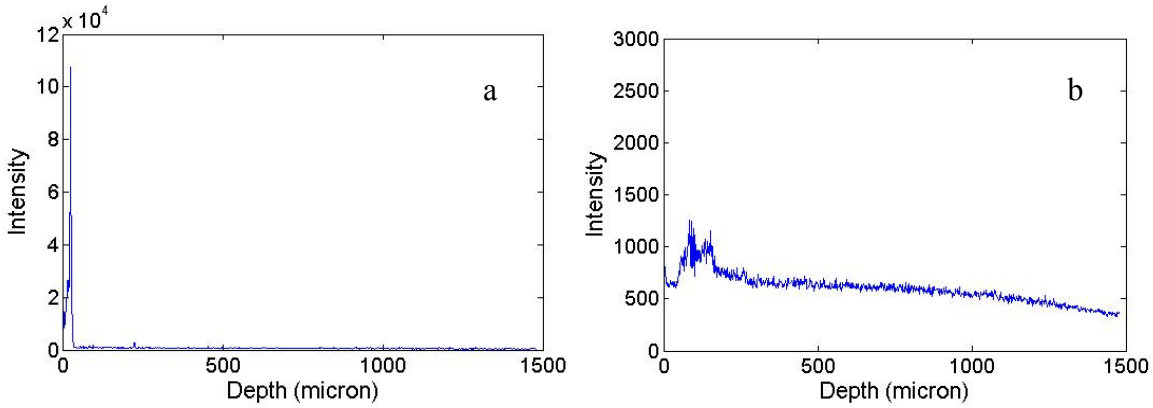

FIGURE 2.13 Averaged PSFs for SNR measurement. a, OCM signal from the mirror; b, Same measurement with the reference arm blocked.

2.3.3 Co-registered NLOM-OCM image

To demonstrate the co-registered NLOM-OCM images, collagen matrix gels with cultured cells were made as previously described. [38] Stable human umbilical vein endothelial cells (HUVEC, Cambrex, Charles City, IA) expressing green fluorescent protein were generated using a recombinant lentivirus system (Invitrogen, Carlsbad, CA). The fibrous collagen gels were assembled to 2.5 mg/ml before incorporating 1μM S1P. Monolayer of HUVECs were seeded on the top of the 3D collagen gel, added M199 media with growth factor (VEGF+FGF+RSII+Ascrobic acid+TPA), and the culture was fixed after 72 hours. The co-registered NLOM-OCM images of this sample are shown in Figure 2.14. The OCM image in Figure 2.14A detected the back-reflected light from the sample and is sensitive to the differences in refractive index. For this sample both the cell and collagen matrix can be seen in the OCM image. While SHG and TPEF in NLOM are sensitive for the collagen and cells respectively, as shown in Figure 2.14 B

and C. These co-registered images of NLOM-OCM showed that this setup can image complementary information of the sample.

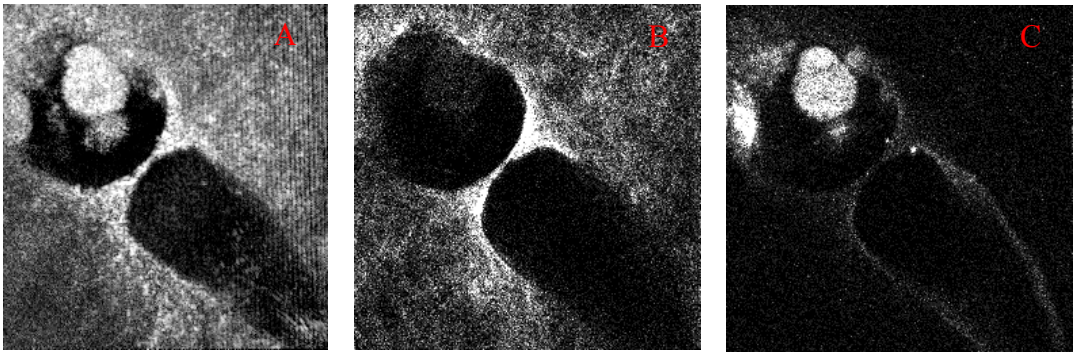

FIGURE 2.14 Co-registered NLOM-OCM images of cells in collagen matrix. A OCM, B SHG, C TPEF.

2.4 Discussion

A Fourier domain OCM system was built and integrated into an existing custom-built NLOM system utilizing a sub-10-fs Kerr-lens mode-locked Ti:Al_2O_3 laser as a common source. These pulses are an order of magnitude shorter in duration than what is typically used in NLOM systems and results in an order of magnitude improvement in peak power (for a given pulse energy) with which to generate nonlinear optical signals for image rendering. For two-photon processes such as SHG, the improvement in signal generation scales as the inverse pulse duration; for two-photon excited fluorescence, signal generally follows this same relationship but will ultimately depend on the overlap between the pulse two-photon excitation and molecular (two-photon) absorption

spectrum. [30] However, optical resolution or sampling volume of NLOM remains dependent on how tightly the laser is focused by the microscope objective.

The use of sub-10-fs pulses ensures co-registration of the NLOM and OCM images. Whereas lateral resolution of the modalities is limited by diffraction, axial resolution of OCM is determined to a first approximation by the coherence length of light. Thus, in integrating NLOM and OCM with a common source, its coherence length, which is inversely proportional to bandwidth, should compare with the confocal parameter of the focusing objective. For the 40×, 0.8 NA objective used in our measurements, the confocal parameter is ~1.9 μm (Rayleigh approximation) which compares well with the 2.12 μm coherence length of the laser.

2.5 Conclusion

In conclusion, a Fourier domain OCM was integrated with an existing NLOM system. This combined NLOM-OCM system showed the capability of imaging different components of the sample simultaneously. In the next chapters this NLOM-OCM setup was used to image cornea anatomy and swelling process and to measure both the microstructural and mechanical response of rabbit cornea to changes of IOP as a function of depth.

CHAPTER III

RABBIT CORNEA IMAGING USING COMBINED NONLINEAR OPTICAL MICROSCOPY-OPTICAL COHERENCE MICROSCOPY SYSTEM

3.1 Introduction

3.1.1 Cornea microstructure

From the anterior to posterior, cornea can be divided into 5 layers: epithelium, Bowman's layer, stroma, Descemet's membrane, and endothelium. Figure 3.1 shows a H&E staining histology image of rabbit cornea. We can clearly see the different layers within the rabbit cornea. The corneal stroma comprises most of the cornea thickness and can be further divided into three portions: anterior, mid, and posterior stroma.

3.1.1.1 Epithelium

The epithelium layer in rabbit cornea has a thickness of about 40μm and contains three cell types: basal cells, wing cells, and superficial cells. The basal cells are the only epithelial cells that can undergo mitosis. [39] The daughter cells then push to the cornea surface and change their shapes to form the wing and superficial cells. Scanning electron microscopy (SEM) has been used to image cornea microstructure and showed no significant difference between human and rabbit cornea epithelium. [40] Numerous nerve fibers randomly perforate through corneal epithelium. These fibers sometimes branch two or more times immediately before penetrating through the epithelium.

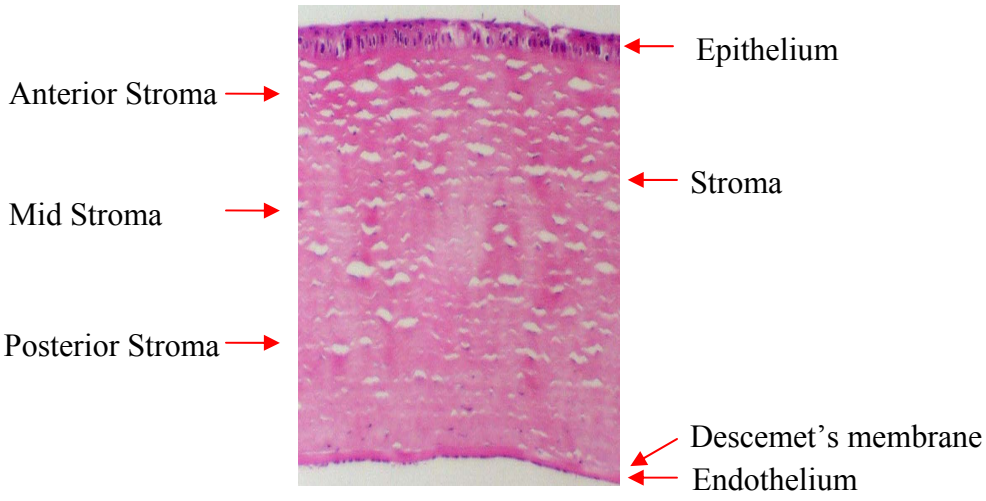

FIGURE 3.1 Histology image of rabbit cornea.

Confocal reflectance microscopy has also been used to image cornea structure. For human cornea epithelium, confocal imaging has shown wing cells with bright nuclei and basal cells with dark cytoplasm and bright cell boundaries. [41] Confocal images of rabbit cornea epithelium showed superficial cells with a polygonal and sometimes hexagonal shape and the cytoplasm and cell nuclei can be visualized. [42] Basal cells showed dark cytoplasm, bright cell boundaries, and no cell nuclei. The basal cells are smaller than superficial cells and tightly organized.

3.1.1.2 Bowman's layer

Bowman's layer is composed of amorphous material between the epithelium and stroma with a thickness of 8-12 μm. Some species like rabbit do not have Bowman's layer. Bowman's layer does not regenerate after injury. The main component of Bowman's layer is collagen fibrils. In contrast to the stroma in which the collagen fibrils are well

organized, the collagen fibrils in Bowman's layer are randomly arranged and their diameters are about two-thirds that of those in the stroma. [39]

3.1.1.3 Stroma

Stroma comprises about 90% of cornea thickness and about 71% of the dry weight of cornea. [39] It is composed of several hundred layers of collagen lamellae each composed of collagen fibrils of uniform diameter. These collagen fibrils are parallel to each other within each lamella but make large angles with those in adjacent lamellae.

The collagen lamellae structure is very important for providing the tensile and cohesive strength for cornea. Several techniques, including SEM, X-ray scattering, and SHG, have been used to characterize the collagen lamellae organization in the stroma. Collagen lamellae extend from limbus to limbus and are oriented at various angles to each other. The lamellae frequently branch out in 2 or 3 lamellae in the same or adjacent layer. In the anterior stroma, the collagen lamellae are narrower and have an interwoven structure. Posterior stroma collagen lamellae have an orthogonal structure. This depth dependent collagen structure accounts for several different cornea properties at different depth. For example, it has been found that the anterior stroma is highly resistant to corneal swelling. [43] In the plane parallel to cornea surface, collagen lamellae are aligned orthogonally at the center and circumferentially at the edge. [8]

Between collagen lamellae are keratocytes and nerve fibers. The keratocytes occupy 3-5% of the stromal volume and are parallel to cornea surface. Their function is to maintain the collagen fibrils and extracellular matrix. [39] Cellular processes leave the nuclear region at all angles and sometimes connect to those of a neighboring keratocytes.

These interactions with neighboring keratocytes are important to the regulation of cell function.

There are some stromal neural plexus with different diameters in corneal stroma. [40] This plexus often contact with keratocyte bodies and has higher density in the rabbit than in the human cornea. But no difference in density was found between anterior and posterior stroma in both rabbit and human corneas.

Confocal microscopy has been used to image the keratocyte nuclei and corneal nerves in the stroma[42] and found that the density of keratocytes is significantly higher in the anterior stroma in rabbit cornea.

3.1.1.4 Descemet's membrane

Descemet's membrane is a basement membrane secreted by the endothelium with a thickness of about 10μm. Descemet's membrane has two layers: anterior banded layer and posterior nonbanded layer. In rabbit central cornea, the anterior layer is a continuous plate of parallel fibers, while the posterior layer is discontinuous and is formed by parallel bundles of fibers. The fibers of these two layers cross each other at about 110º. [40]

3.1.1.5 Endothelium

Endothelium is a single layer of cells with a thickness of 4-6 μm. The endothelial cells have a flattened hexagonal shape and are about 20 μm wide. The endothelium is very important for cornea function like hydration. The endothelial cells can enlarge the cell size and maintain tight apposition with neighboring cells to prevent aqueous humor into the stroma. [39] Confocal reflectance microscopy can image the endothelial cells with bright cell bodies and dark cell boundaries without visible cell nuclei. [42]

3.1.2 SHG imaging of collagen structure in corneal stroma

The primary feature of a typical collagen molecule is its triple-stranded helical structure, in which three collagen polypeptide chains (α-chains) are wound around one another. [44] Collagens are mainly composed of proline and glycine. Proline stabilizes the helical conformation in each α-chain, while glycine is regularly spaced at every third residue throughout the central region of the α-chain. As the smallest amino acid, glycine allows the three helical α-chains to pack tightly together to form the final collagen superhelix.

Until now, about 25 collagen α-chains have been identified. Although a lot of types of triple-stranded collagen molecules could be assembled from these collagen α-chains, only a small number of types have been found. The main types of collagen found in connective tissues are types 1,2,3,5, and 11, which are the fibrillar collagens, or fibril-forming collagens. These collagen molecules can assemble into collagen fibrils, which are thin structures (10-300nm in diameter). Collagen fibrils often aggregate into collagen fibers, which normally have a diameter of several micrometers. Corneal collagen fibrils are mainly composed of type 1 collagen molecules together with type 5 collagen molecules. [45]

The triple-helix structure in collagen makes it a noncentrosymmetric structure, which satisfies a condition for SHG. SHG from collagen was first reported by Fine and Hansen[46] in 1971. The first 3D collagen structure in cornea stroma using SHG imaging was shown by Yeh et al[47] in 2002. Since then, SHG has been utilized to study the collagen structure in the cornea. [48-50] Compared to the other techniques, SHG can image the collagen structure in cornea stromal lamellae in situ without fixing, sectioning, or

staining. As described in previous chapter, SHG is a coherent process. Thus polarized SHG can be used to differentiate collagen fiber orientation. [47, 51, 52]

SHG signal from collagen in cornea can be detected either in forward- or backward-scattering configuration. The collagen structure showed different structures with these two detection configurations. [53, 54] The forward detected signals showed distinct collagen fibrils and have relatively strong SHG signals, while backward detected SHG signals are more diffuse with relatively weak SHG signals and cannot resolve the individual collagen fibrils very clearly. Normally there is no correlation between the forward and backward detected collagen structure.

SHG has been used to differentiate normal and diseased cornea. Morishige et al, [55] using 3D reconstructed SHG images, showed that in both normal and edematous human corneas, collagen lamellae are interwoven in the anterior stroma and Bowman's layer. However 12 months after the onset of edema, subepithelial fibrosis began to develop. In keratoconus corneas, 3D SHG images of collagen showed less interwoven structure at anterior stroma and an obvious reduction of lamellae that insert into the Bowman's layer.[56] Genetically induced collagen alternations which are possibly due to the collagen synthesis and deposition in the transgenic mice corneal stroma has been observed using SHG imaging. [57] Matteini et al[51] analyzed the photothermally-induced collagen structure loss in corneal stroma using SHG images. The damage to the collagen structure in diseased cornea can also be quantified. Rao et al used Fourier transform SHG to measure the 'preferred' orientation and maximum spatial frequency of the collagen fibers in porcine corneal stroma. [58]

SHG has been used to evaluate the intrastromal ablation effect[59] and determine its threshold. [60] Wang et al[61] used both SHG and TPEF to evaluate the outcomes of laser refractive surgeries and observe the wound healing during follow up checks.

SHG can be combined with other optical imaging techniques to image both collagen and other components in the cornea. For example, Chen et al [62] combined SHG with reflective confocal imaging to visualize both collagen and cells (epithelial and keratocytic) in bovine cornea sequentially.

3.1.3 OCM imaging of rabbit cornea

Back reflection of incident laser light, primarily from corneal epithelia, endothelia, and keratocytes, has been used to study cornea anatomical structure and physiological activity with confocal reflectance microscopy. [39, 41, 42, 63-65] OCM is an analogous technique to confocal reflectance microscopy that detects backscattered laser light interferometrically and thus could be used to image cornea anatomy and physiological activity similar to confocal reflectance microscopy. Although OCT has been widely used to study different aspects of cornea, [66-72] very few studies used OCT/OCM to study cornea anatomy. The only study that has been reported used full-field OCT to image the different components within human donor cornea. [73] They observed the structures of epithelial cells, Bowman's layer, keratocytes, nerve fibers, Descemet's membrane, and endothelial cells. The keratocyte cytoplasm, nuclei, processes, and the 2D interconnectivity of the keratocytes were also visualized using this setup.

In this chapter the developed integrated NLOM-OCM system based on a Kerr-lens mode-locked sub-10-fs Titanium:Sapphire laser was used to study rabbit cornea anatomy and swelling process. With NLOM, endogenous nonlinear optical signals from cells (two-photon excited fluorescence from pyridine nucleotides and flavoproteins) and collagen (second harmonic generation, SHG) have been used to image cornea anatomy in normal [47, 53] and diseased states [74] and to characterize collagen microstructural response to changes in IOP. [75] Back reflection of incident laser light, primarily from corneal epithelia, endothelia, and keratocytes, has been used in elegant experiments with confocal microscopy that showed activated keratocytes following photorefractive keratectomy was the origin of corneal haze. [76] Here, the NLOM-OCM system is shown to be sensitive to cornea anatomical structures and hydration state without using exogenous markers or labels.

3.2 Methods and materials

Corneas from New Zealand white rabbits (male, about 13 weeks, 2-3 kg weight) were used in this experiment and visibly transparent before, during, and after NLOM measurements. All experiments were performed on corneas less than 48 hours post-mortem. Isolated corneas with a scleral rim were mounted on an artificial anterior chamber (K20-2125, Ketena Products, Denville, NJ) for pressure control and imaging. A rubber o-ring was placed on the chamber surrounding the mounted cornea to facilitate water coupling with the microscope objective. The base of the chamber has two ports with silicone tubing, in-line pinch clamps and female luer-lok connectors. One port was

connected to a syringe filled with phosphate buffered saline to control hydrostatic pressure. A manometer was connected in series on the second port for accurate pressure readings. The pressure was set to 5 mmHg to image the cornea anatomy and study the cornea swelling process. During the imaging of cornea anatomy, 4% dextran 70 was added to the phosphate buffered saline to prevent cornea swelling. During swelling experiments, no dextran was added. The NLOM-OCM setup that was described in Chapter II was then used to image the cornea sample.

3.3 Results

3.3.1 Cornea anatomy

Complementary endogenous contrast mechanisms of integrated NLOM-OCM enable the imaging of rabbit cornea anatomy without exogenous stains or dyes. Representative NLOM-OCM images are shown in Figure 3.2 of the different layers of rabbit cornea. Both backreflected light [41, 42, 77] and two-photon excited fluorescence [78] may be used in OCM and NLOM, respectively, to image the cobblestone morphology of the epithelium (Fig. 3.2A). However, because of their different contrast mechanisms, OCM and NLOM show complementary cell features. OCM signal is derived from backscattered light making it sensitive to changes in refractive index. Highlighted in OCM images of the epithelium are cell membrane and some nuclei (Fig 3.2A, top). In contrast, two-photon excited fluorescence from factors related to the cell metabolic cycle (pyridine nucleotides and flavoproteins) is localized to the cytoplasm leaving dark nuclei and cell membranes (Fig 3.2A, bottom).

NLOM-OCM images from the underlying matrix of the epithelium are shown in Fig. 3.2B. The morphology of the basal lamina imaged by OCM (Fig 3.2B, top) was consistent with that shown by confocal reflectance microscopy [64]. Weak SHG signal was detected from the collagen anchoring fibrils using NLOM (Fig 3.2B, bottom) in contrast to the collagen lamellae of the stroma. In the stroma, keratocyte nuclei (stars) and nerve fibers (arrows) were visualized by OCM (Fig. 3.2C, top), and collagen lamellae were imaged using SHG by NLOM (Fig. 3.2C, bottom). Between the stroma and endothelium, Descemet's Membrane was marked by an absence of SHG signal from fibrillar collagen (data not shown) and the presence of nerve fibers as observed by OCM (see Fig. 3.2D). The endothelium was revealed with OCM in Fig. 3.2E by high contrast between bright cell bodies and dark cell membranes.

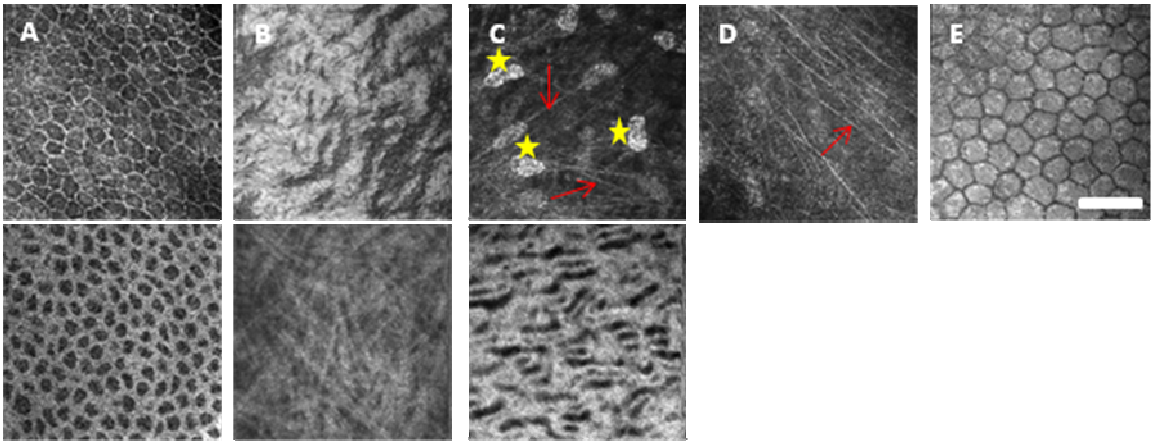

FIGURE 3.2 Representative NLOM (lower)-OCM (upper) images of rabbit cornea at different depths. A Epithelium, B epithelial-stromal boundary, C Stroma, D Descemet's Membrane, and E Endothelium. Scale bar is 40 μm.

3.3.2 Cornea swelling

Confocal reflectance microscopy has been used previously to reveal different keratocyte morphologies for corneas in the swollen state versus normal hydration. [7] Whereas keratocyte nuclei were prominent in normally hydrated corneas, nuclei and extended processes were revealed in swollen corneas and attributed to some combination of changes in keratocyte hydration and in refractive index of the surrounding matrix. Similar observations of keratocyte morphology are made with OCM depending on cornea hydration state. Nuclei of stromal keratocytes were observed with OCM in normally hydrated corneas whereas the whole cell body with extended processes became visible with corneal swelling. This dynamic was shown for a single keratocyte in Figure 3.3 as a function of swelling time. In Figure 3.3A, the cornea was normally hydrated and only the keratocyte nucleus was visible. The intact cornea was exposed to phosphate buffered saline and swelled with time. As the cornea swelled, extended processes of the keratocyte became visible as shown in Figures 3.3B-D. This effect of swelling on keratocyte morphology was used as a real time indicator of corneal hydration during NLOM-OCM measurements.

An advantage of the integrated NLOM-OCM system is that the keratocyte network of swollen corneas can be imaged in the context of stromal collagen lamellae and segmented as shown in Figures 3.3E-G. The keratocyte network of a swollen cornea imaged by OCM is shown in Figure 3.3E. An NLOM image from the same field-of-view was acquired simultaneously of the collagen matrix using SHG and shown in Figure 3.3F. Green and red false colors were applied to the OCM and NLOM images,

respectively, and overlayed in Figure 3.3G to reveal the interrelationship between the keratocyte network and underlying collagen matrix.

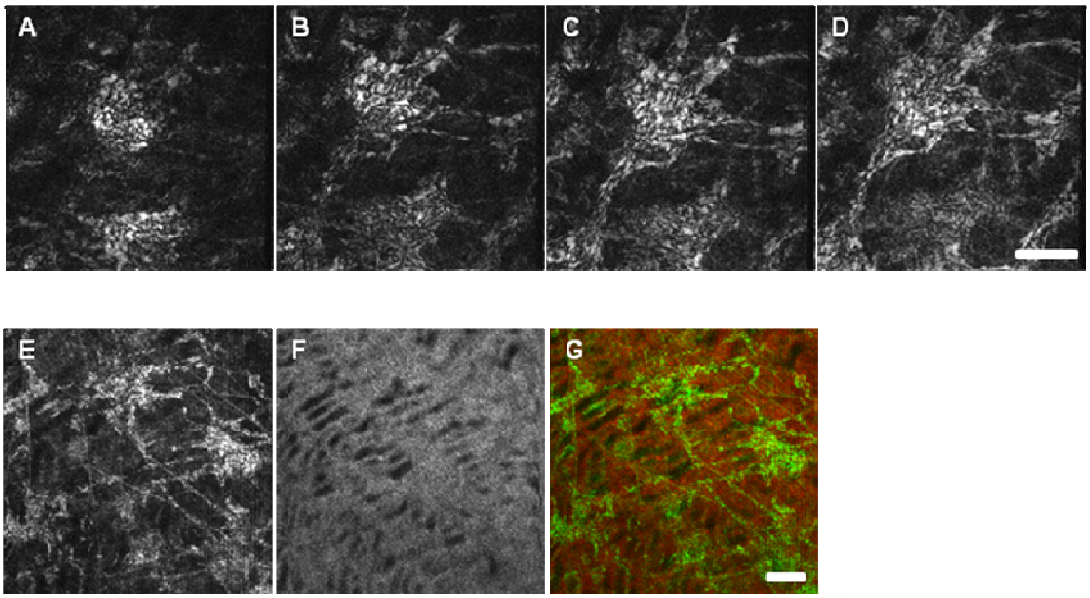

FIGURE 3.3 Keratocytes morphology changes with cornea swelling. Top row: OCM images of same keratocyte with different hydration states. A Normal hydration state, B-D Increased hydration states. Bottom row: Co-registered NLOM-OCM images. E OCM image, F SHG image, G Overlay image. Scale bars are 20 μm.

3.4 Discussion and conclusion

Combined NLOM-OCM is shown to be sensitive to cornea anatomical structures and hydration state without using exogenous markers or labels. Major components of the rabbit cornea were imaged including cells (epithelial, keratocytic, and endothelial), nerve fibers and extracellular matrix, especially the collagen lamellae. This anatomical information can be used to characterize physiological state of the cornea. For example, keratocyte morphology was used as an experimental indicator of cornea hydration state.

OCM visualization of keratocyte nuclei was shown to expand to include the cell body and processes with corneal swelling. Under normal hydration, keratocyte nuclei were highly scattering compared with the cell body. Light scattering may be mitigated in the cell body by balance of refractive indices between the cell cytoplasm and extracellular environment. Within the cell body, the refractive index may be regulated by crystallin proteins. [79] Upon swelling, the balance in refractive index between the extracellular environment and crystallin regulated cytoplasm may be disrupted resulting in the heightened OCM signal from keratocyte cell body and extended processes. Our data suggest, though it were not quantified, that swelling results in changes in intra- and extracellular refractive indices as observed in the OCM image of keratocyte network and faint extracellular matrix in Figure 3.3E.

CHAPTER IV

CORNEA MICROSTRUCTURAL RESPONSE MEASURED USING NONLINEAR OPTICAL MICROSCOPY*

4.1 Introduction

The mechanical response of the cornea is believed to be dominated by the properties of collagen lamellae in the stroma. The stroma comprises ~90% of the cornea full thickness and largely determines the tissue's physical properties. This was demonstrated by mechanical tests of rabbit and human corneas that showed their stress-strain curves followed that of the stroma rather than that of Descemet's membrane.[1] Follow-on biomechanical measurements have delineated non-uniform cornea material properties along the meridian and between epithelial and endothelial surfaces.[2, 3] However, measuring the corneal mechanical response as a function of depth has been difficult, but could prove informative, for example, in improving efficacy and increasing the eligible patient pool for elective laser refractive surgeries. Biomechanical measurements require placement of fiducial markers that are used to measure strain with applied IOP. Therefore, depth-dependent mechanical response cannot be characterized using traditional biomechanical testing without disturbing the corneal structure.

---

*Reprinted with permission from "Rabbit Cornea Microstructure Response to Changes in Intraocular Pressure Visualized by using Nonlinear Optical Microscopy" by Q. Wu and A.T. Yeh, 2008, Cornea, 27, 2, 202-208, Copyright *@2008Lippincott Williams & Wilkins.*

The underlying structural basis for the mechanical properties of the cornea, and the stroma in particular, has been well characterized by electron and x-ray microscopy. [80] Mechanical response and maintenance of cornea shape and refractive function are interrelated with stromal composition and microstructural organization. Epithelial and endothelial cell layers also act to regulate stromal material properties (e.g., hydration). The microstructural architecture of the cornea is heterogeneous and anisotropic, resulting in non-uniform material properties. [80]

Heterogeneous mechanical behavior across the meridional surface was believed to result from anisotropy in collagen lamellar organization.[2, 3] X-ray diffraction studies have shown preferential collagen lamellae orientations in medial-lateral/superior-inferior and circumferential directions in central and limbal regions, respectively. [81] Electron microscopy studies of local lamellae orientation have found predominantly circumferential regions in posterior limbus of human cornea. [9] Along the anterior-posterior axis, regional differences in lamellar packing were believed to be responsible for observed inhomogeneous tissue swelling. [9, 10, 43] In the anterior third, electron microscopy studies have shown anterior-posterior interweaving in addition to planar branching of lamellae that is believed to fortify mechanical strength for maintaining corneal curvature.[10, 43] Interweaving lamellae architecture in the midstroma of human cornea has been observed using scanning electron microscopy when stretched along the anterior-posterior axis following ground substance removal. [9, 82] This interweaving architecture could be the basis for interlamellar cohesive strength. [4, 83, 84] Distribution of cross-angles in the mid and anterior stroma have been measured radially by region and

found to have a different orientational preference than that of the posterior. [9] Collagen lamellae in posterior stroma were believed to be well ordered and branched parallel to the plane of curvature. This heterogeneous lamellae architecture suggested a microstructural basis for inhomogeneous stromal mechanical response as a function of depth that may impact corneal interventions.

Laser scanning confocal microscopy can provide microstructural and biological information in vivo [85] and has been used in longitudinal studies of biological response following photorefractive keratectomy to understand the origins of corneal haze. [76, 79] In a novel application of confocal reflectance microscopy, light scattering from cell nuclei was used to image their movement as a function of IOP and depth through the full thickness. [7] Maximal posterior strains were measured to be larger than anterior strains in normally hydrated and swollen rabbit cornea which was an intuitive result assuming an incompressible tissue. However, how collagen lamellae accommodate changes in IOP remains an open question. Without the use of exogenous stains or dyes, endogenous signals used for corneal imaging in confocal [7, 64, 76, 85-87] and two-photon excited fluorescence microscopy [47, 59] originate from cells that constitute only ~5% of the cornea by volume.

For NLOM, SHG in collagen can be used to specifically image stromal lamellae in situ without fixing, sectioning or staining. [47, 48, 53, 59, 88] Combined with its ability to render thin images from within thick tissues, NLOM may be used to visualize 3D collagen morphology in individual corneas as a function of IOP. Hypotensive corneas have morphological features in the stroma that can be characterized by an absence of

collagen which we refer to as interlamellar gaps. [47, 48] These features are present through the full thickness of the stroma, decrease in size with increasing IOP as a function of depth and can be used as an indirect measure of mechanical response depth profile. Views from reconstructed 3D images rendered from NLOM suggest these interlamellar gaps result from interlaced anterior-posterior and planar oriented lamellae.

4.2 Methods and materials

4.2.1 Cornea preparation

Corneas (n = 20) from New Zealand white rabbits (male, about 13 weeks, 2-3 kg weight) were used in this experiment and prepared similarly to the method described in Section 3.2. Corneas were clamped at the sclera imparting artificial boundary conditions. However, the clamping geometry of the chamber minimized stress on the sclera[89] and measured changes in thickness and microstructural morphology with pressure were repeatable and reversible. Before each imaging experiment, corneas were preconditioned through a pressure cycle (5 to 30 mmHg) three times.

4.2.2 NLOM setup

NLOM of the combined NLOM-OCM system has been described in detail in Chapter II. Corneas were allowed to equilibrate for 10 minutes at each IOP before acquisition of NLOM images.

4.2.3 Image processing

Grayscale color map was adjusted to cover the histogram of each en face NLOM intensity image shown. Image stacks through the full thickness of central cornea were

acquired and used to reconstruct 3D visualization. Each 16-bit NLOM image was normalized (to 255), converted to 8-bit, Tagged Image File Format and input to MetaVue (V6.2r4, Universal Imaging Corp., Downingtown, PA) and AutoVisualize (v93, AutoQuant Imaging, Inc., Silver Spring, MD) for 3D reconstruction. Cross-sectional views were captured from 3D renderings. For specified cross-sectional views (see the figure on page 59), nonlinear background subtraction was applied to adjust for non-uniform signal intensity through the central cornea cross-section. This operation applied a 10 X 10 pixel sliding window within which the minimum intensity value was subtracted from the first pixel. The window operated on every pixel of cross-sectional image incrementally; for operations within 10 pixels of image edge, the window was filled with values mirror-reflected across the image boundary.

4.3 Results

Hypotensive corneas have distinct morphological, collagen lamellae patterns. Collagen specific NLOM imaging using SHG revealed these morphological features through the cornea full thickness which can be characterized by an absence of collagen, or interlamellar gaps. [47] These gaps presumably consisted of water and ground substance. Representative NLOM images of collagen lamellae morphology are shown in Figures 4.1A & B from mid and posterior central stroma of hypotensive corneas (IOP = 5 mmHg; scale bar is 20 μm). Predominant collagen fiber angles are revealed in each image as well as distinct collagen morphology at 250 μm (Figure 4.1A) and 570 μm (Figure 4.1B) below the surface. The midstroma had irregular collagen morphology as

shown in Figure 4.1A. Regular collagen morphology is revealed in posterior stroma with parallel lamellae of high aspect ratio in the image plane between gaps (see Figure 4.1B). The orientation of parallel lamellae with high aspect ratio changed at different depths (data not shown).

Stromal collagen morphology changed in response to increasing IOP. NLOM images of the same field of view using SHG in collagen are shown from the mid (Figure 4.1A, D, and E) and posterior stroma (Figure 4.1B, G, and H) at pressures of 5, 8, and 20 mmHg. The anterior stroma was not shown because of its sensitivity to IOP; at 8 mmHg, collagen morphology of the anterior stroma did not reveal interlamellar gaps, providing no obvious tomographic features to co-register IOP data sets. The NLOM images from the mid and posterior central cornea were representative of the microstructural response through the full thickness: collagen morphology showed decreasing gap area with increasing IOP. As suggested previously, the morphological response was dependent on depth. Anterior central stroma showed high sensitivity to increasing IOP and morphological features persisted in posterior stroma even at hypertensive IOP (see Figure 4.1E).

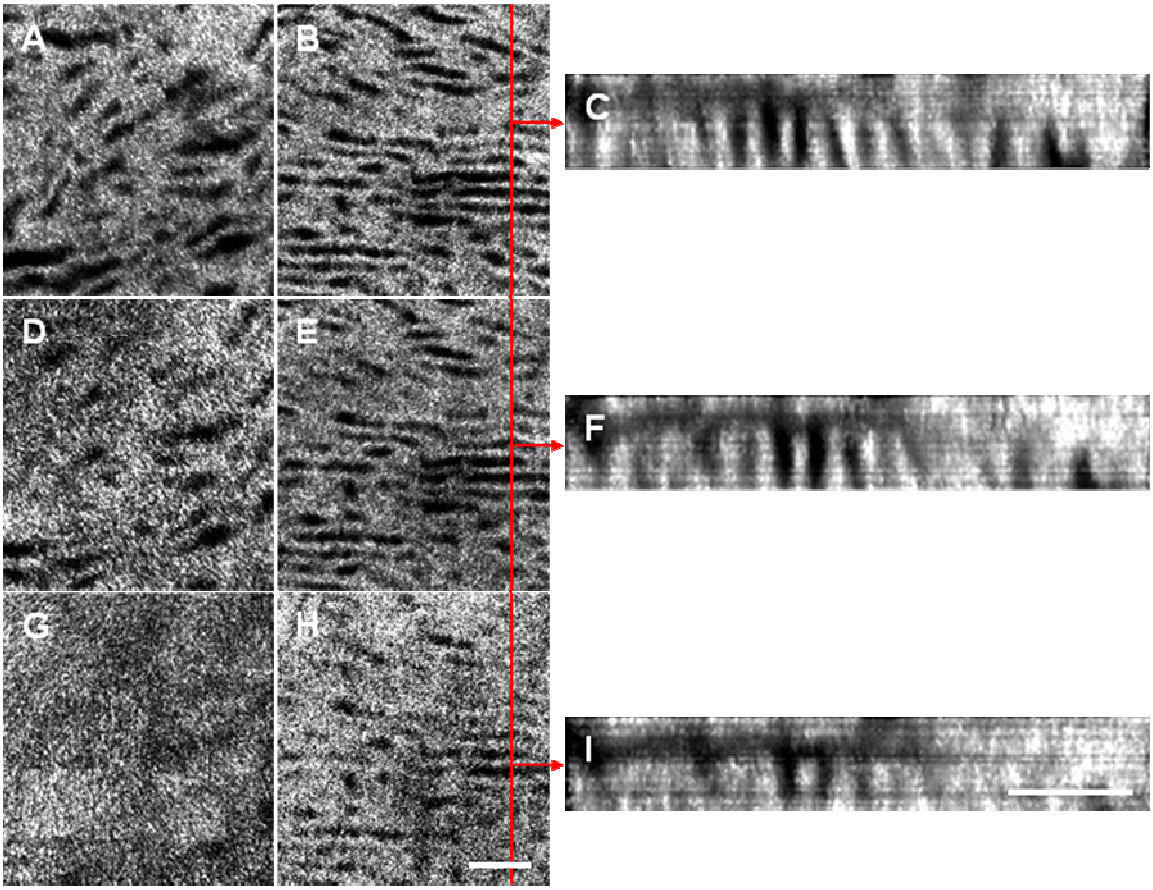

FIGURE 4.1 Collagen morphology of mid and posterior stroma as a function of intraocular pressure (5 mmHg: A, B, C; 8 mmHg: D, E, F; 20 mmHg: G, H, I). Cross-sectional views from posterior (C, F, I) are denoted in *en face* images (B, E, H) by red line. Red arrows denote positions of *en face* images (B, E, H) in cross-sectional views (C, F, I). Scale bars are 20 μm.

NLOM image stacks were used to reconstruct 3D renderings from which cross-sectional views of collagen morphology were obtained from posterior stroma at 5, 8, and 20 mmHg. The image stack was acquired with 0.5 μm increments in depth. The images shown in Figures 4.1C, F, and I correspond to cross-sectional views of Figures 4.1B, E and H at the position denoted by the red line (scale bar is 20 μm).

For reference, the positions of the 2D NLOM images are denoted in the cross-sectional views by red arrows. The cross-sectional view at 5 mmHg revealed high aspect ratio collagen lamellae oriented along the anterior-posterior axis (see Figure 4.1C). With increasing IOP, the aspect ratio of collagen lamellae oriented along the anterior-posterior axis decreased (collagen lamellae thickened), resulting in a reduction in interlamellae area as shown in Figure 4.1F & I.

The collagen microstructural response of the central cornea to increasing IOP was quantified as a function of depth. NLOM image stacks were acquired through the full thickness of the central stroma with a step size of 5 μm at five different IOPs (5, 8, 10, 15, and 20 mmHg). Each NLOM image was normalized by the intensity distribution from a homogeneous sample (fluorescent slide) before manual thresholding. Morphological features were quantified by calculating the fraction of pixels with SHG signal in each 256 X 256 NLOM image. The full thickness was divided into 10 layers, and the fraction of pixels with SHG signal was averaged from NLOM images in each layer. The fractional area without collagen is shown in the bar graph in Figure 4.2 as a function of IOP and dimensionless depth (n = 5 corneas). For each pressure, the fractional interlamellar gap area increased with depth. In addition, the morphological response to increasing IOP was observed to be more dramatic in anterior than posterior stroma. The ratio between fractional interlamellar gap area measured at 5 and 20 mmHg was >100:1 in contrast to 3:1 in the anterior and posterior regions, respectively.

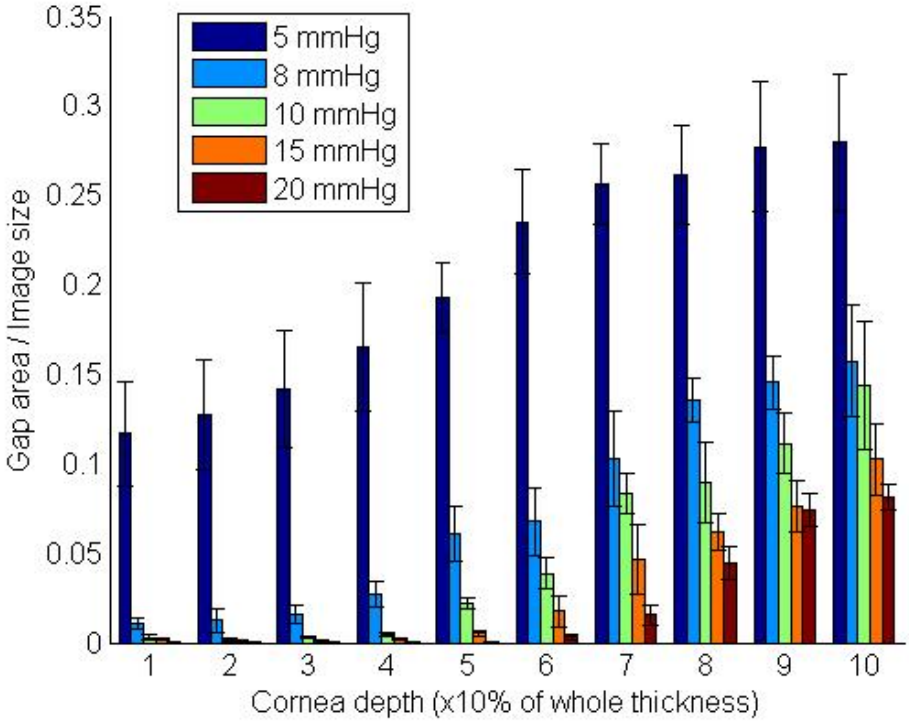

FIGURE 4.2 Fractional interlamellar gap area as a function of normalized depth and intraocular pressure.

The evolution of collagen microstructure in a single (central) cornea is shown in Figure 4.3 as a function of IOP (5, 7, 10, 15, and 20 mmHg). The full thickness, cross-sectional images were processed with the nonlinear background subtraction routine described earlier. Twenty-one planar lamellae are labeled at 5 and 20 mmHg to aid in following their progression as a function of IOP. Six lines are drawn between corresponding lamellae at each pressure as guides to the eye. Central corneal stroma thickness decreases with increasing IOP, from 430 to 300 μm for this specimen. Changes in thickness with IOP are inhomogeneous with depth with the largest (smallest) observed in the posterior (anterior).

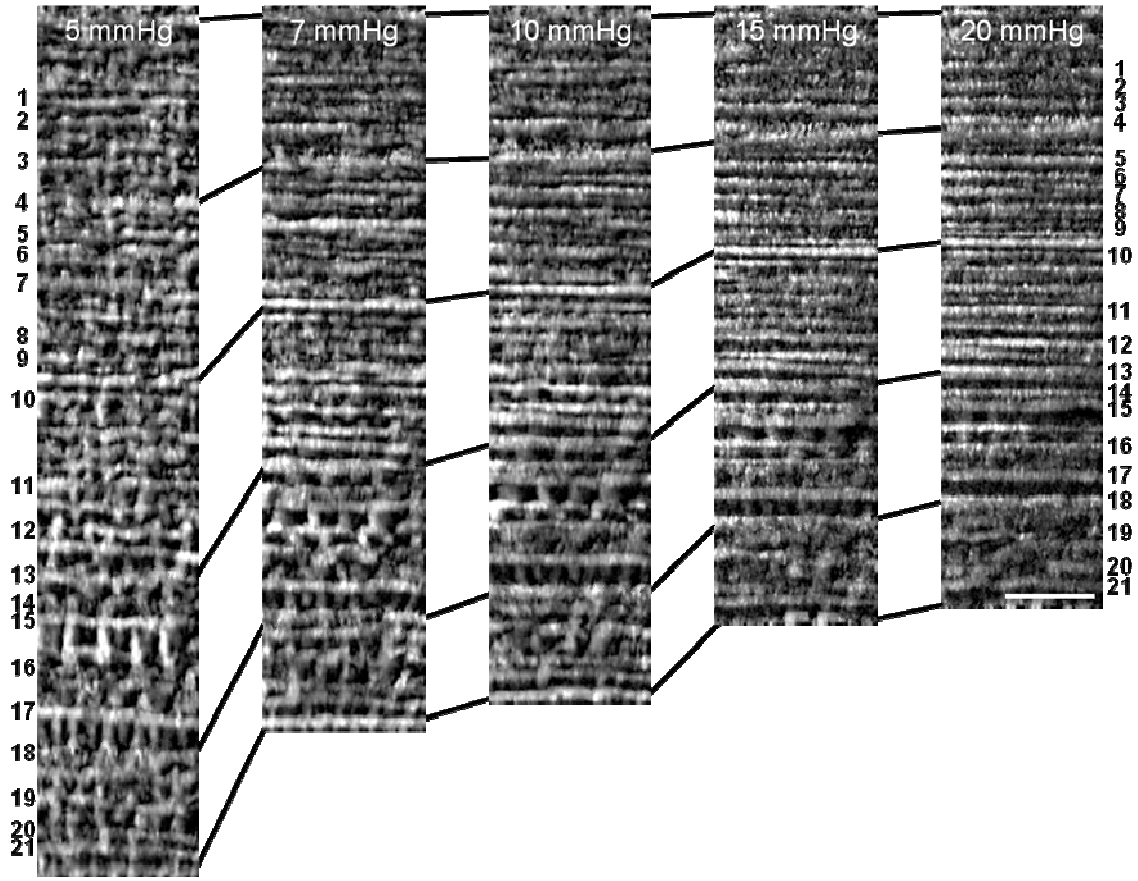

FIGURE 4.3 Cross-sectional views of collagen lamellae through full thickness of central cornea as a function of IOP. Lines connect corresponding lamellae at each pressure. Twenty-one lamellae are labeled to aid in following their progression with IOP. Scale bar is 50 μm.

4.4 Discussion

In this study, SHG was used to specifically image collagen lamellae 3D organization in rabbit central corneal stroma[47, 48, 53, 59, 88] as a function of IOP. The ability to acquire thin, microscopic images with minimal sample processing (i.e., without fixing, sectioning, or staining) was used to visualize collagen lamellae accommodation of changes in IOP within individual, intact rabbit corneas. Interlamellar gaps, characterized by the absence

of collagen, were a prominent morphological feature throughout the full thickness of hypotensive corneas and have been observed previously using NLOM. [47, 48] In contrast to this previous work, this study suffered from corneal swelling but showed that these interlamellar gaps originated from interlaced planar and transverse collagen lamellae. In addition, in situ NLOM imaging of microstructural 3D organization while cornea IOP was increased to normal and hypertensive states can be used to reconcile observed transverse collagen segments[9, 10, 53, 82] with the prevailing view of layered lamellae stromal architecture in the plane of the tissue. [43, 80, 81, 90-94] Transverse collagen lamellae through the central cornea full thickness may also explain the observation that the cohesive strength of layered lamellae was independent of the depth at which it was measured. [4]

The observation of transverse collagen lamellae in hypotensive corneas in this study was accentuated by its state of hydration. Hypotensive corneas had thicknesses $t > 430$ μm as measured by NLOM. The effects of swelling on cornea thickness may be reminiscent of previous experiments that reported interlaced collagen lamellae using electron microscopy. [9, 82] In these experiments, cornea preparation for electron microscopy included NaOH treatment for ground substance removal and physically stretching the tissue along the anterior-posterior axis. The same mechanical effect may have been achieved with corneal swelling under hypotension, albeit with minimal disruption to the native structure.

The NLOM measured depth-dependent, morphological response to increasing IOP suggested that the anterior stroma was less compliant than deeper regions. The short (~5

μm) transverse collage segments intertwined with planar lamellae observed in NLOM cross-sectional views may form the structural basis for this rigidity. This is consistent with previous studies that concluded the specific architecture of the most anterior layers was responsible for maintaining corneal curvature.[43] Based on its NLOM measured morphological response, the central cornea may be divided into three regions: the anterior, which is characterized by short transverse collagen lamellae and immediate loss of interlamellar gaps with increasing IOP; mid stroma, which is characterized by medium length transverse collagen lamellae (~25 μm); and posterior, which is characterized by the longest transverse collagen lamellae observed by NLOM (~50 μm) and persistence of interlamellar gaps even at hypertensive IOP (>20 mmHg). It is interesting to note that the posterior fractional interlamellar gap area showed negligible change for IOP > 20 mmHg, consistent with confocal reflectance microscopy measured mechanical tests of the cornea within intact rabbit globes that showed stiffened response (negligible strain) for IOP $\geqslant$ 20 mmHg. [7]

Present understanding of the heterogeneous and anisotropic mechanical properties of the cornea have been derived from disparate measurements of tissue biomechanics and ultrastructure performed under different conditions and sample preparations. We submit, based on the results presented herein, that NLOM using SHG in collagen may provide an avenue to simultaneously measure regional mechanical response and the underlying tissue microstructure. It remains an open question whether clamping the scleral rim affected the observed microstructural response of the central cornea. Clamping geometry is certainly important; the boundary conditions imposed by the

artificial anterior chamber used here has been shown to allow for repeatable and reproducible corneal responses, e.g., swelling. [89] Nevertheless, the results do demonstrate an ability to visualize cornea microstructural response to incremental changes in IOP and NLOM could be combined with, for example, confocal reflectance microscopy to measure regional strain. [7] It would be instructive to repeat these measurements in enucleated globes or in vivo and to map the corneal mechanical response through the limbal region and into the adjacent sclera.

4.5 Conclusion

SHG from NLOM reveals interwoven collagen lamellae sheets through the full thickness of rabbit central cornea oriented along the anterior-posterior axis and parallel with the surface. Non-destructive nature of NLOM allows 3D imaging of stromal architecture as a function of IOP *in situ*. Collagen morphological features were used as an indirect measure of depth-dependent mechanical response to changes in IOP.

CHAPTER V

CORNEA MECHANICAL RESPONSE MEASURED USING OPTICAL COHERENCE MICROSCOPY

5.1 Introduction

The mechanical properties of the cornea play a central role to its multifaceted function of serving as both a physical barrier and the primary refractive element in the eye. Yet, our present understanding of its mechanical response and underlying microstructural basis is derived from disparate measurements of tissue biomechanics and ultrastructure performed under different conditions and sample preparations. Indeed, cornea biomechanics have been found to affect seemingly routine intraocular pressure (IOP) measurements which appear to correlate with central cornea thickness and curvature, though in a non-straightforward manner as to preclude a simple correction for applanation tonometry. Also, sophisticated ablation algorithms used to predict corneal response to refractive surgeries remain largely empirical, underscoring the need for better understanding of—or, at least, the need for technologies that can characterize—cornea mechanical properties in situ.

Traditionally, tissue mechanical properties are characterized by testing measurements that track the displacement of fiducial markers with applied loads. [1-3] For intact cornea, the placement of exogenous markers is limited to the epithelial or endothelial surface. However, the stroma comprises more than 90% of the cornea thickness and preferred orientations of the collagen lamellae in the superior-inferior and

nasal-temporal directions in the central and circumferential orientation in the limbal regions suggest anisotropic mechanical response. [3, 8] Furthermore, there is accumulating evidence that the stroma is mechanically heterogeneous including ultrastructural measurements that showed more isotropic distribution of collagen lamellae in the anterior third compared with the posterior two-thirds, [95] measurements of central cornea collagen microstructural response to changes in IOP that exhibited differences among the anterior, mid, and posterior regions,[75] and swelling experiments that attributed the maintenance of corneal curvature to a comparatively stiff anterior third relative to the posterior two-thirds.[43]

Confocal reflectance microscopy has been used to measure anterior and posterior (endothelial) mechanical response with a similar experimental design as reported here. [7] OCM is an analogous technique to confocal reflectance microscopy that detects backscattered laser light interferometrically. In this chapter, OCM is used to characterize central cornea mechanical response as a function of depth layer by layer using keratocyte nuclei as endogenous fiducial markers. The depth dependent cornea mechanical response is correlated with the depth dependent cornea collagen structure and its response to IOP from NLOM results.

5.2 Methods and materials

5.2.1 Cornea preparation

Corneas (n = 7) from New Zealand white rabbits (male; ~13 weeks; weight, 2-3 kg) were used in this experiment and prepared similarly to the method described in Section

4.2.1. The only difference is that 4% dextran 70 was added to the phosphate buffered saline in this study to prevent cornea swelling. Swelling was also monitored in real-time using keratocyte morphology, see Figure 3.3 in page 48.

5.2.2 OCM setup

Fourier domain OCM setup in the NLOM-OCM system has been described in Chapter II. Corneas were allowed to equilibrate for 10 minutes at each IOP before acquisition of OCM images.

5.2.3 Strain calculation

Central cornea strain was calculated from OCM full thickness image stacks from 8 corneas at 5 different IOPs (5, 8, 10, 15, and 20 mmHg). The cornea was aligned for repeated measure of the same corneal features at all 5 pressures. The coordinates of centroids for 3 cell nuclei were identified at all 5 IOPs at each depth. To find nuclei centroids, a rectangular region around each cell nucleus was selected and a mean filter of 5 X 5 sliding window applied. A threshold was used to determine the boundary and the geometric center was calculated based on this boundary. Strain was calculated by nuclei displacement from their coordinates imaged at 5 mmHg. Using the coordinates of three nuclei in both the reference ($\Delta\mathbf{X}$) and deformed state ($\Delta\mathbf{x}$), the deformation gradient $\mathbf{F}$ was calculated by

$$\Delta\mathbf{x} = \mathbf{F} \cdot \Delta\mathbf{X}. \tag{5.1}$$

Green's strain $\mathbf{E}$ was calculated using

$$\mathbf{E} = \frac{1}{2}\left(\mathbf{F}^T\mathbf{F} - \mathbf{I}\right). \tag{5.2}$$

To compare the strains at different depths, the corneal stroma was subdivided into 10 equal thickness layers and the values $\|\mathbf{E}\|$ in each layer were averaged,

$$\|\mathbf{E}\| = \sqrt{trace(\mathbf{E} \cdot \mathbf{E}^T)}\,. \qquad (5.3)$$

5.2.4 Statistical analysis

In both the strain and structural (gap area) depth distribution data, the whole corneal stroma was divided into ten layers. To statistically determine which layers of tissue have similar properties, MATLAB software (The Mathworks, Natick, MA) was used to perform a k-means clustering analysis on the strain and structural depth distribution at five different pressures with the assumption that the whole corneal stroma can be grouped as three different regions.

5.3 Results

In our approach to characterizing the biomechanics of the central cornea, mechanical testing of the cornea was implemented by measuring the in-plane displacement of keratocyte nuclei as a function of IOP. OCM was used to measure nuclei displacement layer by layer through the full thickness of the stroma. Our methodology is illustrated in Figure 5.1 for a given layer from within the central region of a rabbit cornea. Three keratocyte nuclei were tracked within a field of view at 5 pressures, 5 (Fig. 5.1A), 8 (Fig. 5.1B), 10 (Fig. 5.1C), 15 (Fig. 5.1D) and 20 mmHg (Fig. 5.1E). Coordinates of the keratocyte centroids were found from boundaries defined for the nuclei and used to calculate displacement at each pressure relative to the reference pressure of 5 mmHg. Where possible, sampling was increased by tracking multiple nuclei (up to five) and

calculating in-plane displacements among sets of three. Full thickness image stacks acquired with 1 μm increments were subdivided into 10 layers by depth. Calculated displacements were averaged for each layer.

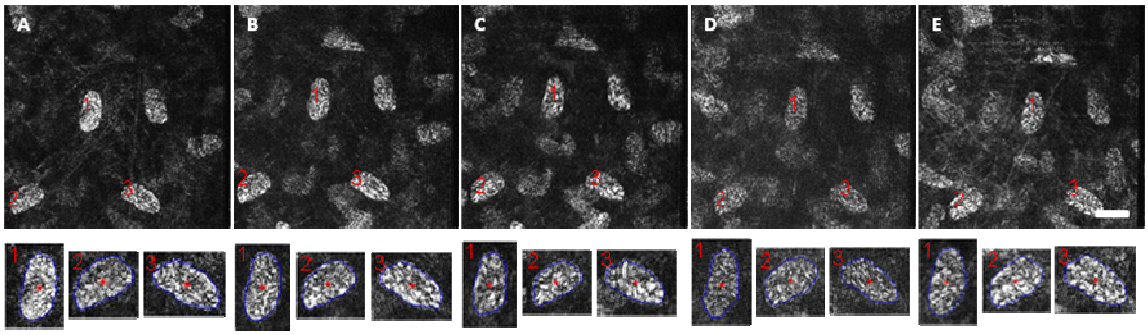

FIGURE 5.1 Illustration of cell nuclei center identification and track of cell nuclei movement with the changes of IOPs. A 5 mmHg, B 8 mmHg, C 10 mmHg, D 15 mmHg, and E 20 mmHg. Scale bar is 20 μm.

In-plane (Green's) strain with IOP was calculated from the measured displacements and plotted as a function of depth in Figure 5.2A. Ten mechanical response curves are shown, each corresponding to one of the 10 subdivided layers of the full thickness and numbered sequentially from the anterior. The results showed that the strain at each pressure increased with depth and that the mechanical response curves were nonlinear. Error bars are standard deviations calculated from averaging measurements from seven corneas. It is interesting to note that this depth-dependent mechanical response corresponds with the collagen microstructural response to changes in IOP in Figure 4.2. To compare these two results, gap area versus pressure is shown in Figure 5.2B. Again each curve corresponds to one of the 10 subdivided layers numbered

from anterior as in Figure 5.2A. We then applied a statistical analysis using k-means clustering on both the strain and structural (gap area) depth distribution at the five different pressures as described in section 5.2.4. Strain and structural depth distribution can be grouped into three groups as anterior 20%, mid 40%, and posterior 40%, and anterior 40%, mid 30%, and posterior 30%, respectively.

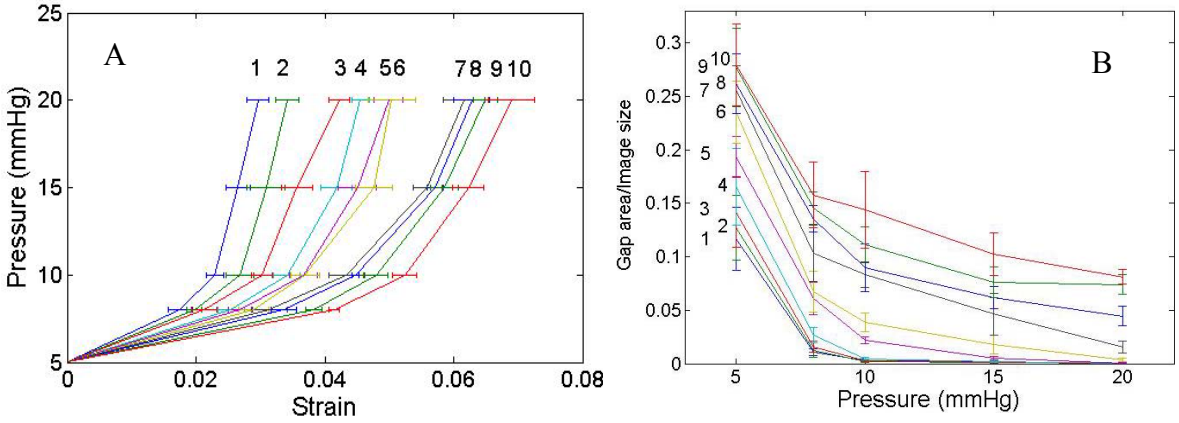

FIGURE 5.2 Cornea strains (A) and structural (gap area) response (B) distribution at different depths.

5.4 Discussion and conclusion

5.4.1 Cornea mechanical response measured using OCM

In this study, the OCM results from the developed NLOM-OCM system was used to measure the depth-dependent mechanical response of rabbit central cornea. A traditional mechanical testing approach was used where (in-plane) displacement between fiducial markers was measured as a function of applied force, in this case IOP. Keratocyte nuclei were used as endogenous markers[7] that enabled layer by layer characterization in situ

without destruction of tissue. [96] It should be noted that only keratocyte nuclei displacement were measured in this study which limited biomechanical characterization to the stroma between the basal lamina and Decement's membrane. Based on the contrast observed from NLOM-OCM images of the epithelium and endothelium, extending these mechanical testing measurements to those layers, as done previously with exogenous markers, [1-3] should be straight forward.

Depth-dependent mechanical response curves were nonlinear and exhibited three distinct regions, anterior 20%, mid 40%, and posterior 40%. Typically, a cell nucleus has an area of about 800 pixels and the coordinates of nuclei centroids were repeatable to within one-tenth of a pixel. The displacements were measured between nuclei separated by tens of micrometers. Thus, more than 60 pixels separated centroids in typical measurements with displacements of about three pixels. Indeed, these results were consistent with previous mechanical tests that showed larger posterior than anterior strains. [3, 7] In particular, strains presented here were close to the results in Maurice's [1] measurement of rabbit cornea stains at the epithelial surface, considering that we used the sum of the two principle strains calculated from the in-plane Green's strains. Also, results presented here were measured on isolated cornea with scleral rim mounted on an artificial anterior chamber versus whole globe with 20-gauge needle inserted into the anterior chamber. Artificial boundary conditions may be imposed with the artificial anterior chamber by clamping of the scleral rim, but it may have minimal effect on the central corneal region of study.

Current biomechanical models of the cornea employ finite element methods because of the tissue's complicated geometry and have incorporated nonlinear response and predominant collagen fiber orientations. [97, 98] By incorporating nonlinear response and predominant fiber orientations, heterogeneous and anisotropic response along the meridian can be described. The results presented herein can further inform these models with quantitative characterization of the mechanical response depth profile, albeit limited to the central region. Moreover, the approach and methodology demonstrated here can be used to completely characterize corneal mechanical properties (with depth) within intact globes along principal directions of the meridian. This direct measure of cornea mechanical response will be vital in understanding its biomechanical properties.

5.4.2 Correlation between cornea microstructural and mechanical response using combined NLOM-OCM

To correlate the cornea mechanical response depth profile with collagen structure in cornea stroma, cross-sectional views of collagen lamellae through the full thickness of the central corneal stroma using SHG from NLOM are shown in Figure 5.3 of a swollen (A-D) and normally hydrated (E-H) cornea at 5 and 20 mmHg (scale bar is 50 μm). The cross-sectional views (Figure 5.3 A, C, E, and G) were captured from 3D reconstructions of NLOM image stacks acquired with 0.5 μm increments. These cross-sectional views were input to a nonlinear background subtraction routine (see Section 4.2.3) to compensate for non-uniform signal intensity acquired through the full thickness of the stroma; the resultant images are shown in Figure 5.3 B, D, F, and H adjacent to the originals. With IOP of 5 mmHg, planar and transverse oriented collagen lamellae were

observed through the full thickness as seen in Figure 5.3 A, B, E, and F. In addition, anterior-posterior interweave of planar collagen lamellae was observed in the anterior stroma. The full thickness of the cross-sectional view shown was measured to be 410 μm in normally hydrated and 550 μm in swollen cornea using NLOM. In mid to posterior stroma, transverse collagen lamellae appeared regularly spaced in both corneas and accentuated in the swollen cornea. Cross-sectional views revealed that the length of transverse collagen lamellae varied with depth: in the swollen cornea, segments were observed as long as 50 μm in posterior, 25 μm in mid and as short as 5 μm in anterior stroma.

Upon pressurization to 20 mmHg, central cornea thickness was observed to decrease and collagen lamellae assumed predominantly planar orientation as seen in Figure 5.3 C, D, G, and H. However, anterior-posterior interweave and transverse collagen lamellae were still evident in the anterior and posterior stroma, respectively. From Figure 5.3 D, the planar collagen lamellae numbered >100 through the full thickness (t = 410 μm) of the swollen stroma.

The marked differences in mechanical response exhibited by the anterior, mid, and posterior central cornea correlate with microstructural organization of the collagen lamellae. The anterior 30% and posterior 40% of cornea stroma at low pressure of 5 mmHg are demarked by dotted lines in Figure 5.3 A, B, E, and F. Small strains of the anterior (top 20%) in Figure 5.2A correspond with interlaced lamellae and short ($\leqslant$5 μm) transverse collagen segments that were best viewed at low tension particularly in swollen corneas (see Figure 5.3 B). large strains of the posterior 40% in Figure 5.2A

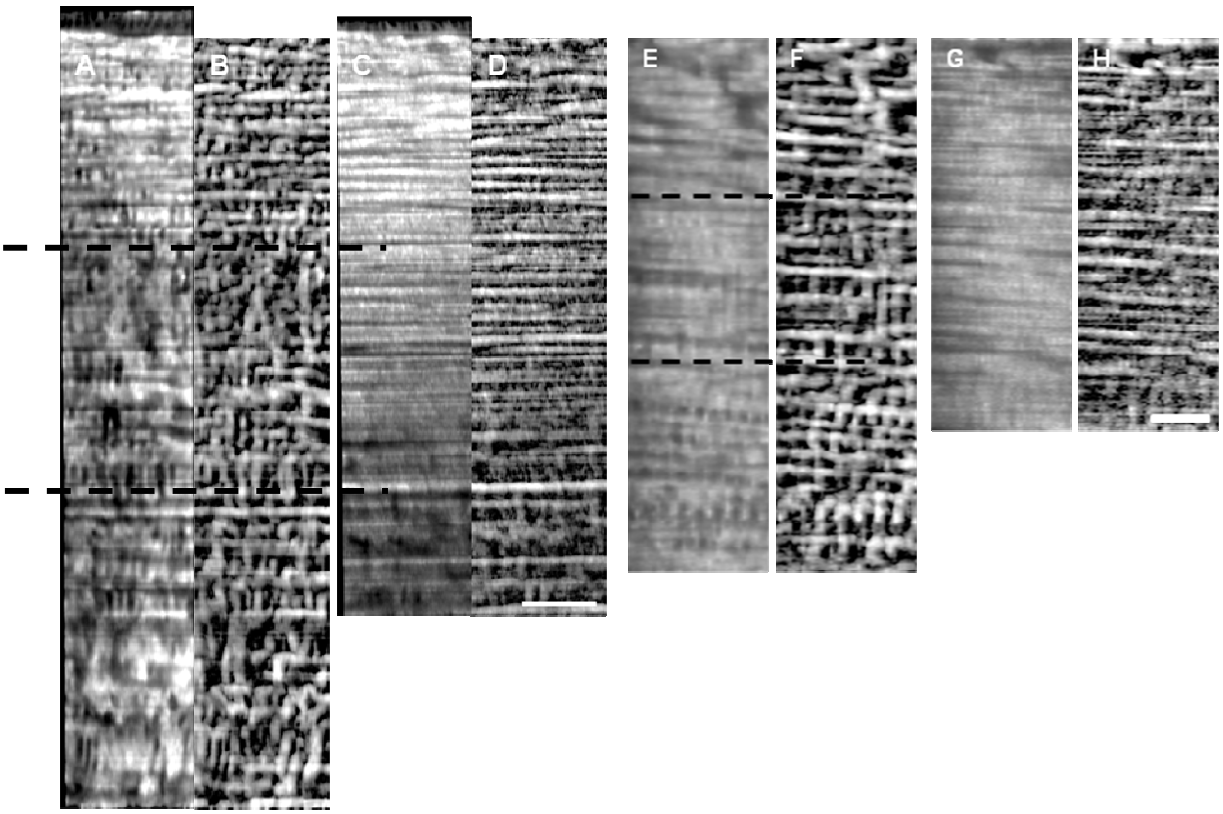

FIGURE 5.3 Cross-sectional views of collagen lamellae through full thickness of stroma in swollen (A-D) and normally hydrated (E-F) central cornea at 5 mmHg (A, B, E, F) and 20 mmHg (C, D, G, H). Nonlinear background subtraction was used to compensate for non-uniform signal intensity across the full thickness (B, D, F, H). Scale bar is 50 μm.

correspond with the collagen organization of regularly organized, long transverse segments of the posterior stroma.

The measured mechanical response depth profile also correlates with previous measurements of collagen lamellae response to the changes in IOP in Chapter IV. Characteristic of stromal collagen morphology particularly at low tension were interlamellar collagen-free spaces or gaps. As a fraction of the NLOM image area, these gaps decreased with increased IOP in a depth dependent manner. Anterior gaps were

characterized by an immediate decrease in fractional area in contrast with posterior gaps which persisted even at hypertensive IOP, as shown in Fiugre 4.2 and 5.2B. Between the mechanical response study here and the previous collagen microstructural response study, there was a slight mismatch in the characterization of the anterior stroma, 20% versus 40%, respectively. Otherwise, the correlation between the two studies was remarkable given the limited number of samples (12 corneas).

CHAPTER VI

SUMMARY AND FUTURE WORK

In this study a Fourier domain optical coherence microscopy (OCM) system was integrated into an existing nonlinear optical microscopy (NLOM) system. This combined NLOM-OCM system was used to image cornea anatomy and the swelling process. In addition, this NLOM-OCM system provided a means to simultaneously measure the cornea microstructural and mechanical response to the changes of intraocular pressure (IOP) as a function of depth. The results correlated depth dependent collagen structure and its response to IOP with strain in rabbit cornea stroma.

In this study only the central cornea was studied and only the deformation gradient (**F**) was measured and used to calculate the Green strain (**E**) depth distribution. To predict how cornea will respond to the changes of cornea tissue, tissue elasticity (**K**) at different locations in the cornea from center to edge need to be measured as cornea is heterogeneous. The next step of this research will be to image several positions along the meridional and diagonal directions to attain a complete profile of cornea mechanical properties. To measure cornea tissue elasticity, we first need to determine the strain energy density (**W**) of the tissue. The strain energy density can be described as a function of deformation gradient with certain parameters that can be determined from either experimental calibration[97] or numerical fit using inverse finite element method. [99] The stress (**S**) and elasticity then can be calculated using the following equations:

$$\mathbf{S} = 2\frac{\partial \mathbf{W}}{\partial \mathbf{C}} \tag{6.1}$$

$$\mathbf{K} = 2\frac{\partial \mathbf{S}}{\partial \mathbf{C}} \tag{6.2}$$

where $\mathbf{C} = \mathbf{F}^T\mathbf{F}$. Thus based on the experimental results of $\mathbf{F}$ and the defined $\mathbf{W}$, the elasticity of cornea tissue can be measured and a mathematical model developed to simulate cornea tissue response to changes of cornea structure, which ultimately can be used in the development of algorithms for laser refractive surgeries suitable for each individual patient.

REFERENCES

1. Jue B, Maurice DM. The mechanical properties of the rabbit and human cornea. *J Biomech* 1986;19:847-853.

2. Shin TJ, Vito RP, Johnson LW, McCarey BE. The distribution of strain in the human cornea. *J Biomech* 1997;30:497-503.

3. Hjortdal JO. Regional elastic performance of the human cornea. *J Biomech* 1996;29:931-942.

4. Maurice DM, Monroe F. Cohesive strength of corneal lamellae. *Exp Eye Res* 1990;50:59-63.

5. McPhee TJ, Bourne WM, Brubaker RF. Location of the stress-bearing layers of the cornea. *Invest Ophth Vis Sci* 1985;26:869-872.

6. Hollman KW, Emelianov SY, Neiss JH, Jotyan G, Spooner GJR et al. Strain imaging of corneal tissue with an ultrasound elasticity microscope. *Cornea* 2002;21:68-73.

7. Hennighausen H, Feldman ST, Bille JF, McCulloch AD. Anterior-posterior strain variation in normally hydrated and swollen rabbit cornea. *Invest Ophth Vis Sci* 1998;39:253-262.

8. Aghamohammadzadeh H, Newton RH, Meek KM. X-ray scattering used to map the preferred collagen orientation in the human cornea and limbus. *Structure* 2004;12:249-256.

9. Radner W, Zehetmayer M, Aufreiter R, Mallinger R. Interlacing and cross-angle distribution of collagen lamellae in the human cornea. *Cornea* 1998;17:537-543.

10. Komai Y, Ushiki T. The 3-dimensional organization of collagen fibrils in the human cornea and sclera. *Invest Ophth Vis Sci* 1991;32:2244-2258.

11. McDonald MB, Kaufman HE, Frantz JM, Shofner S, Salmeron B, Klyce SD. Excimer laser ablation in a human eye. *Arch Ophthalmol-Chic* 1989;107:641-642.

12. Pallikaris IG, Papatzanaki ME, Siganos DS, Tsilimbaris MK. A corneal flap technique for laser insitu keratomileusis - human studies. *Arch Ophthalmol-Chic* 1991;109:1699-1702.

13. Roberts C. The cornea is not a piece of plastic. *J Refract Surg* 2000;16:407-413.

14. Roberts C. Biomechanics of the cornea and wavefront-guided laser refractive surgery. *J Refract Surg* 2002;18:S589-S592.

15. Shahinian L. Laser-assisted subepithelial keratectomy for low to high myopia and astigmatism. *J Cataract Refr Surg* 2002;28:1334-1342.

16. Pallikaris LG, Naoumidi II, Kalyvianaki MI, Katsanevaki VJ. Epi-LASIK: comparative histological evaluation of mechanical and alcohol-assisted epithelial separation. *J Cataract Refr Surg* 2003;29:1496-1501.

17. Litwin KL, Moreira H, Ohadi C, McDonnell PJ. Changes in corneal curvature at different excimer laser ablative depths. *Am J Ophthalmol* 1991;111:382-384.

18. Amm M, Duncker GIW. Refractive changes after phototherapeutic keratectomy. *J Cataract Refr Surg* 1997;23:839-844.

19. Stark WJ, Chamon W, Kamp MT, Enger CL, Rencs EV, Gottsh JD. Clinical follow-up of 193-Nm ArF excimer laser photokeratectomy. *Ophthalmology* 1992;99:805-812.

20. Maiman TH. Stimulated optical radiation in Ruby. *Nature* 1960;187:493-494.

21. Einstein A. Quantum theory of radiation. *Phys Z* 1917;18:121-128.

22. Moulton PF. Spectroscopic and laser characteristics of Ti-Al_2O_3. *J Opt Soc Am B* 1986;3:125-133.

23. Franken PA, Weinreich G, Peters CW, Hill AE. Generation of optical harmonics. *Phys Rev Lett* 1961;7:118-119.

24. Freund I, Deutsch M, Sprecher A. Connective-tissue polarity - optical 2nd-harmonic microscopy, crossed-beam summation, and small-angle scattering in rat-tail tendon. *Biophys J* 1986;50:693-712.

25. Campagnola PJ, Loew LM. Second-harmonic imaging microscopy for visualizing biomolecular arrays in cells, tissues and organisms. *Nat Biotechnol* 2003;21:1356-1360.

26. Meshulach D, Silberberg Y. Coherent quantum control of two-photon transitions by a femtosecond laser pulse. *Nature* 1998;396:239-242.

27. Goppert-Mayer M. Elementary file with two quantum fissures. *Ann Phys-Berlin* 1931;9:273-294.

28. Kaiser W, Garrett CGB. 2-Photon excitation in CaF_2 - Eu^{2+}. *Phys Rev Lett* 1961;7:229-231.

29. Denk W, Strickler JH, Webb WW. Two-Photon laser scanning fluorescence microscopy. *Science* 1990;248:73-76.

30. Pang S, Yeh AT, Wang C, Meissner KE. Beyond the 1/Tp limit: two-photon-excited fluorescence using pulses as short as sub-10-fs. *J Biomed Opt* 2009;14.

31. Meshulach D, Silberberg Y. Coherent quantum control of multiphoton transitions by shaped ultrashort optical pulses. *Phys Rev A* 1999;60:1287-1292.

32. Zipfel WR, Williams RM, Webb WW. Nonlinear magic: multiphoton microscopy in the biosciences. *Nat Biotechnol* 2003;21:1368-1376.

33. Masters BR, So PTC. The genesis of nonlinear microscopies and their impact on modern developments. In: Masters BR, So PTC, eds. *Handbook of Biomedical Nonlinear Optical Microscopy*. New York: Oxford University Press; 2008:5-28.

34. Izatt JA, Hee MR, Owen GM, Swanson EA, Fujimoto JG. Optical coherence microscopy in scattering media. *Opt Lett* 1994;19:590-592.

35. Huang D, Swanson EA, Lin CP, Schuman JS, Stinson WG et al. Optical coherence tomography. *Science* 1991;254:1178-1181.

36. Fercher AF, Hitzenberger CK, Kamp G, El-Zaiat SY. Measurement of intraocular distances by backscattering spectral interferometry. *Opt Commun* 1995;117:43-48.

37. Larson AM, Yeh AT. Ex vivo characterization of sub-10-fs pulses. *Opt Lett* 2006;31:1681-1683.

38. Lee PF, Yeh AT, Bayless KJ. Nonlinear optical microscopy reveals invading endothelial cells anisotropically alter three-dimensional collagen matrices. *Exp Cell Res* 2009;315:396-410.

39. Klyce SD, Beuerman RW. Structure and function of the cornea. In: Kaufman HE, McDonald MB, Barron BA, eds. *The Cornea.* 2nd ed. London: Butterworth-Heinemann; 1997: 3-50.

40. Ojeda JL, Ventosa JA, Piedra S. The three-dimensional microanatomy of the rabbit and human cornea. A chemical and mechanical microdissection-SEM approach. *J Anat* 2001;199:567-576.

41. Masters BR, Bohnke M. Three-dimensional confocal microscopy of the human cornea in vivo. *Ophthalmic Res* 2001;33:125-135.

42. Labbe A, Liang H, Martin C, Brignole-Baudouin F, Warnet JM, Baudouin C. Comparative anatomy of laboratory animal corneas with a new-generation high-resolution in vivo confocal microscope. *Curr Eye Res* 2006;31:501-509.

43. Muller LJ, Pels E, Vrensen GFJM. The specific architecture of the anterior stroma accounts for maintenance of corneal curvature. *Brit J Ophthalmol* 2001;85:437-443.

44. Alberts B, Johnson A, Lewis J, Raff M, Roberts M, Walter P. *Molecular Biology of the Cell*. New York: Garland Science; 2002: 1096-1097.

45. Holmes DF, Gilpin CJ, Baldock C, Ziese U, Koster AJ, Kadler KE. Corneal collagen fibril structure in three dimensions: structural insights into fibril assembly, mechanical properties, and tissue organization. *P Natl Acad Sci USA* 2001;98:7307-7312.

46. Fine S, Hansen WP. Optical second harmonic generation in biological systems. *Appl Optics* 1971;10:2350-2353.

47. Yeh AT, Nassif N, Zoumi A, Tromberg BJ. Selective corneal imaging using combined second-harmonic generation and two-photon excited fluorescence. *Opt Lett* 2002;27:2082-2084.

48. Teng SW, Tan HY, Peng JL, Lin HH, Kim KH et al. Multiphoton autofluorescence and second-harmonic generation imaging of the ex vivo porcine eye. *Invest Ophth Vis Sci* 2006;47:1216-1224.

49. Wang BG, Koenig K, Riemann I, Krieg R, Halbhuber KJ. Intraocular multiphoton microscopy with subcellular spatial resolution by infrared femtosecond lasers. *Histochem Cell Biol* 2006;126:507-515.

50. Vohnsen B, Artal P. Second-harmonic microscopy of ex vivo porcine corneas. *J Microsc-Oxford* 2008;232:158-163.

51. Matteini P, Ratto F, Rossi F, Cicchi R, Stringari C et al. Photothermally-induced disordered patterns of corneal collagen revealed by SHG imaging. *Opt Express* 2009;17:4868-4878.

52. Stoller P, Reiser KM, Celliers PM, Rubenchik AM. Polarization-modulated second harmonic generation in collagen. *Biophys J* 2002;82:3330-3342.

53. Morishige N, Petroll WM, Nishida T, Kenney MC, Jester JV. Noninvasive corneal stromal collagen imaging using two-photon-generated second-harmonic signals. *J Cataract Refr Surg* 2006;32:1784-1791.

54. Han M, Giese G, Bille JF. Second harmonic generation imaging of collagen fibrils in cornea and sclera. *Opt Express* 2005;13:5791-5797.

55. Morishige N, Yamada N, Teranishi S, Chikama T, Nishida T, Takahara A. Detection of subepithelial fibrosis associated with corneal stromal edema by second harmonic generation imaging microscopy. *Invest Ophth Vis Sci* 2009;50:3145-3150.

56. Morishige N, Wahlert AJ, Kenney MC, Brown DJ, Kawamoto K et al. Second-harmonic imaging microscopy of normal human and keratoconus cornea. *Invest Ophth Vis Sci* 2007;48:1087-1094.

57. Lyubovitsky JG, Spencer JA, Krasieva TB, Andersen B, Tromberg BJ. Imaging corneal pathology in a transgenic mouse model using nonlinear microscopy. *J Biomed Opt* 2006;11: 014013.

58. Rao RAR, Mehta MR, Toussaint KC. Fourier transform-second-harmonic generation imaging of biological tissues. *Opt Express* 2009;17:14534-14542.

59. Han M, Zickler L, Giese G, Walter M, Loesel FH, Bille JF. Second-harmonic imaging of cornea after intrastromal ferntosecond laser ablation. *J Biomed Opt* 2004;9:760-766.

60. Sun H, Han M, Niemz MH, Bille JF. Femtosecond laser corneal ablation threshold: dependence on tissue depth and laser pulse width. *Laser Surg Med* 2007;39:654-658.

61. Wang BG, Riemann I, Schubert H, Schweitzer D, Konig K, Halbhuber KJ. Multiphoton microscopy for monitoring intratissue femtosecond laser surgery effects. *Laser Surg Med* 2007;39:527-533.

62. Chen WL, Sun Y, Lo W, Tan HY, Dong CY. Combination of multiphoton and reflective confocal imaging of cornea. *Microsc Res Techniq* 2008;71:83-85.

63. Ichijima H, Petroll WM, Jester JV, Cavanagh HD. Confocal microscopic studies of living rabbit cornea treated with benzalkonium chloride. *Cornea* 1992;11:221-225.

64. Li HF, Petroll WM, Moller-Pedersen T, Maurer JK, Cavanagh HD, Jester JV. Epithelial and corneal thickness measurements by in vivo confocal microscopy through focusing (CMTF). *Curr Eye Res* 1997;16:214-221.

65. Oliveira-Soto L, Efron N. Morphology of corneal nerves using confocal microscopy. *Cornea* 2001;20:374-384.

66. Drexler W, Morgner U, Ghanta RK, Kartner FX, Schuman JS, Fujimoto JG. Ultrahigh-resolution ophthalmic optical coherence tomography. *Nat Med* 2001;7:502-507.

67. Maldonado MJ, Ruiz-Oblitas L, Munuera JM, Aliseda D, Garcia-Layana A, Moreno-Montanes J. Optical coherence tomography evaluation of the corneal cap and stromal bed features after laser in situ keratomileusis for high myopia and astigmatism. *Ophthalmology* 2000;107:81-87.

68. Bechmann M, Thiel MJ, Neubauer AS, Ullrich S, Ludwig K et al. Central corneal thickness measurement with a retinal optical coherence tomography device versus standard ultrasonic pachymetry. *Cornea* 2001;20:50-54.

69. Baikoff G, Lutun E, Ferraz C. Static and dynamic analysis of the anterior segment with optical coherence tomography. *J Cataract Refr Surg* 2004;30:1843-1850.

70. Grieve K, Paques M, Dubois A, Sahel J, Boccara C, Le Gargasson JF. Ocular tissue imaging using ultrahigh-resolution, full-field optical coherence tomography. *Invest Ophth Vis Sci* 2004;45:4126-4131.

71. Ustundag C, Bahcecioglu H, Ozdamar A, Aras C, Yildirim R, Ozkan S. Optical coherence tomography for evaluation of anatomical changes in the cornea after laser in situ keratomileusis. *J Cataract Refr Surg* 2000;26:1458-1462.

72. Gotzinger E, Pircher M, Sticker M, Fercher AF, Hitzenberger CK. Measurement and imaging of birefringent properties of the human cornea with phase-resolved, polarization-sensitive optical coherence tomography. *J Biomed Opt* 2004;9:94-102.

73. Akiba M, Maeda N, Yumikake K, Soma T, Nishida K et al. Ultrahigh-resolution imaging of human donor cornea using full-field optical coherence tomography. *J Biomed Opt* 2007;12:041202.

74. Tan HY, Sun Y, Lo W, Lin SJ, Hsiao CH et al. Multiphoton fluorescence and second harmonic generation imaging of the structural alterations in keratoconus ex vivo. *Invest Ophth Vis Sci* 2006;47:5251-5259.

75. Wu QF, Yeh AT. Rabbit cornea microstructure response to changes intraocular pressure visualized by using nonlinear optical microscopy. *Cornea* 2008;27:202-208.

76. Moller-Pedersen T, Cavanagh HD, Petroll WM, Jester JV. Stromal wound healing explains refractive instability and haze development after photorefractive keratectomy - a 1-year confocal microscopic study. *Ophthalmology* 2000;107:1235-1245.

77. Petroll WM, Cavanagh HD, Jester JV. 3-dimensional imaging of corneal cells using in-vivo confocal microscopy. *J Microsc-Oxford* 1993;170:213-219.

78. Piston DW, Masters BR, Webb WW. 3-dimensionally resolved Nad(P)H cellular metabolic redox imaging of the in-situ cornea with 2-photon excitation laser-scanning microscopy. *J Microsc-Oxford* 1995;178:20-27.

79. Jester JV, Moller-Pedersen T, Huang JY, Sax CM, Kays WT et al. The cellular basis of corneal transparency: evidence for 'corneal crystallins'. *J Cell Sci* 1999;112:613-622.

80. Bron AJ. The architecture of the corneal stroma. *Brit J Ophthalmol* 2001;85:379-381.

81. Meek KM, Blamires T, Elliott GF, Gyi TJ, Nave C. The organization of collagen fibrils in the human corneal stroma - a synchrotron X-ray-diffraction study. *Curr Eye Res* 1987;6:841-846.

82. Radner W, Mallinger R. Interlacing of collagen lamellae in the midstroma of the human cornea. *Cornea* 2002;21:598-601.

83. Smolek MK, McCarey BE. Interlamellar adhesive strength in human eye bank corneas. *Invest Ophth Vis Sci* 1990;31:1087-1095.

84. Smolek MK. Interlamellar cohesive strength in the vertical meridian of human eye bank corneas. *Invest Ophth Vis Sci* 1993;34:2962-2969.

85. Bohnke M, Masters BR. Confocal microscopy of the cornea. *Prog Retin Eye Res* 1999;18:553-628.

86. Masters BR. Three-dimensional confocal microscopy of the living in situ rabbit cornea. *Opt Express* 1998;3:351-355.

87. Gokmen F, Jester JV, Petroll WM, McCulley JP, Cavanagh HD. In vivo confocal microscopy through-focusing to measure corneal flap thickness after laser in situ keratomileusis. *J Cataract Refr Surg* 2002;28:962-970.

88. Wang BG, Halbhuber KJ. Corneal multiphoton microscopy and intratissue optical nanosurgery by nanojoule femtosecond near-infrared pulsed lasers. *Ann Anat* 2006;188:395-409.

89. Hodson S, Wigham C, Williams L, Mayes KR, Graham MV. Observations on the human cornea invitro. *Exp Eye Res* 1981;32:353-360.

90. Boote C, Dennis S, Huang YF, Quantock AJ, Meek KM. Lamellar orientation in human cornea in relation to mechanical properties. *J Struct Biol* 2005;149:1-6.

91. Maurice DM. The structure and transparency of the cornea. *J Physiol-London* 1957;136:263-286.

92. Meek KM, Fullwood NJ. Corneal and scleral collagens—a microscopist's perspective. *Micron* 2001;32:261-272.

93. Clark JI. Fourier and power law analysis of structural complexity in cornea and lens. *Micron* 2001;32:239-249.

94. Gisselberg M, Clark JI, Vaezy S, Osgood TB. A quantitative evaluation of Fourier components in transparent and opaque calf cornea. *Am J Anat* 1991;191:408-418.

95. Abahussin M, Hayes S, Cartwright NEK, Kamma-Lorger CS, Khan Y et al. 3D collagen orientation study of the human cornea using X-ray diffraction and femtosecond laser technology. *Invest Ophth Vis Sci* 2009;50:5159-5164.

96. Fernandez DC, Niazy AM, Kurtz RM, Djotyan GP, Juhasz T. Finite element analysis applied to cornea reshaping. *J Biomed Opt* 2005;10:064018.

97. Pinsky PM, van der Heide D, Chernyak D. Computational modeling of mechanical anisotropy in the cornea and sclera. *J Cataract Refr Surg* 2005;31:136-145.

98. Pandolfi A, Holzapfel GA. Three-dimensional modeling and computational analysis of the human cornea considering distributed collagen fibril orientations. *J Biomech Eng* 2008;130:061006.

99. David G, Pedrigi RM, Heistand MR, Humphrey JD. Regional multiaxial mechanical properties of the porcine anterior lens capsule. *J Biomech Eng* 2007;129:97-104.

VITA

Name: Qiaofeng Wu

Address: Department of Biomedical Engineering, Texas A&M University
337 Zachry Engineering Center, 3120 TAMU
College Station, TX 77843

Email Address: qfwu@tamu.edu

Education: B.E., Precision Instrument, Wuhan University, China, 2000
M.E., Measurement & Testing Technology and Instrumentation, Wuhan University, China, 2003
Ph.D. Biomedical Engineering, Texas A&M University, 2010